Titan Stratospheric Haze Bands Observed in Cassini VIMS as Tracers of Meridional Circulation

N. W. Kutsop[1] , A. G. Hayes[1,3] , P. M. Corlies[2] , S. Le Mouélic[4] , J. I. Lunine[1] , C. A. Nixon[5] , P. Rannou[6] ,
S. Rodriguez[7] , M. T. Roman[8] , C. Sotin[4,9] , and T. Tokano[10]

The Cassini VIMS Team

[1] Cornell University, 300 Day Hall, Ithaca, NY 14853-2801, USA; nwk25@cornell.edu
[2] Massachusetts Institute of Technology, 77 Massachusetts Avenue, Cambridge, MA 02139-4307, USA
[3] Cornell Center for Astrophysics and Planetary Science, 104 Space Sciences Building, Ithaca, NY 14853, USA
[4] Laboratoire De Planétologie Et Géosciences, 2 Chem. de la Houssinière Bâtiment 4, 44300 Nantes, France
[5] NASA Goddard Space Flight Center, 8800 Greenbelt Road, Greenbelt, MD 20771, USA
[6] Groupe de Spectrométrie Moléculaire et Atmosphérique (GSMA), UMR CNRS 7331, Université de Reims, U.F.R. Sciences Exactes et Naturelles, Moulin de la Housse, B.P. 1039, 51687 Reims Cedex 2, France
[7] Université de Paris, Institut de physique du Globe de Paris, CNRS, 1 Rue Jussieu, 75005 Paris, France
[8] University of Leicester, University Road, Leicester, LE1 7RH, UK
[9] Jet Propulsion Laboratory, 4800 Oak Grove Drive, Pasadena, CA 91109 , USA
[10] Universität zu Köln, Albertus-Magnus-Platz 50923, Köln, Germany

Abstract

We analyzed Cassini data to derive the nature and evolution of circumglobal annuli observed in the stratosphere of Titan, Saturn's largest moon. The annuli were observed between 2004 and 2017 in data acquired by the Visual and Infrared Mapping Spectrometer on board the Cassini spacecraft. We observed a north polar annulus, an equatorial annulus, and several secondary annuli. Pre-Cassini telescopic observations by the Hubble Space Telescope and Keck reported an atmospheric feature consistent with the presence of a south polar annulus between 1999 and 2001, although this feature was not observed by Cassini. Relative to the atmosphere near the annuli, they appear dark at 300–500 nm and bright in methane absorption channels such as the ones at 900 and 1150 nm. The stratosphere seems to rotate around the north pole. Alternatively, it seems to rotate about a point offset from solid-body rotation axis by a few degrees; this point in turn rotates around the solid-body rotation axis.

1. Introduction

Titan has a thick organic haze that obscures its surface at visible and infrared wavelengths and is produced through the dissociation of CH_4 and N_2 by UV light and charged particles (Yung et al. 1984; Lavvas et al. 2008a, 2008b). Noteworthy haze features include a globally extensive thin layer of detached haze (the detached haze layer; Smith et al. 1981; Rages & Pollack 1983; Rannou 2000; Teanby et al. 2009; West et al. 2018; Seignovert et al. 2021), a hemispheric asymmetry in brightness (the north–south asymmetry; Sromovsky et al. 1981; Smith et al. 1982; Tomasko & Smith 1982), and polar hoods that occur during local winter (i.e., the north and south polar hoods; Lorenz et al. 1997; West et al. 2016; Le Mouélic et al. 2018; Seignovert et al. 2021; Penteado et al. 2010). Tracking the distribution and evolution of Titan's haze is a key tool for studying Titan's atmospheric photochemistry, dynamics, and circulation. Herein we describe circumglobal bands, or annuli (Figures 1 and 2), in Titan's atmosphere using observations from Cassini's Visual and Infrared Mapping Spectrometer (VIMS) and discuss their relevance to the nature of Titan's stratosphere and circulation in general. We also used the Cassini Imaging Science Subsystem (ISS) to investigate

links between the annuli seen in VIMS and clouds detected by ISS (Turtle et al. 2018; Figure 2).

Circumglobal bands have been previously identified in Titan's atmosphere. Like the north–south asymmetry, these have been observed to be dark at wavelengths shorter than 600 nm and bright in methane absorption channels such as those at 900 and 1150 nm. North polar atmospheric bands have been previously observed (Smith et al. 1982; Griffith et al. 2008; Jennings et al. 2015; Le Mouélic et al. 2018), and the north polar annulus (NPA) has likely been observed before (Sromovsky et al. 1981; Le Mouélic et al. 2012; Rannou et al. 2012), but not with the morphology and spectral characteristics we report for the first time, which were only possible with near nadir observations of the north pole taken around 2014. The equatorial annulus (EQA) has been previously identified in other works, either directly or indirectly (Roman et al. 2009; de Kok et al. 2010). A south polar annulus (SPA) was observed in Titan's south polar region by Keck and the Hubble Space Telescope (HST; Lorenz et al. 2001; Roe et al. 2002;) prior to Cassini's arrival at Saturn. Throughout the course of the Cassini mission, we did not observe the SPA seen previously.

Circumglobal atmospheric bands are found on all solar system bodies with a substantial atmosphere and are valuable observables for investigating a variety of planetary processes. On Earth and Venus these bands are found in the jet streams, which can be observed by tracking clouds or infrared radiance (Horinouchi et al. 2017). These jets reveal the location of
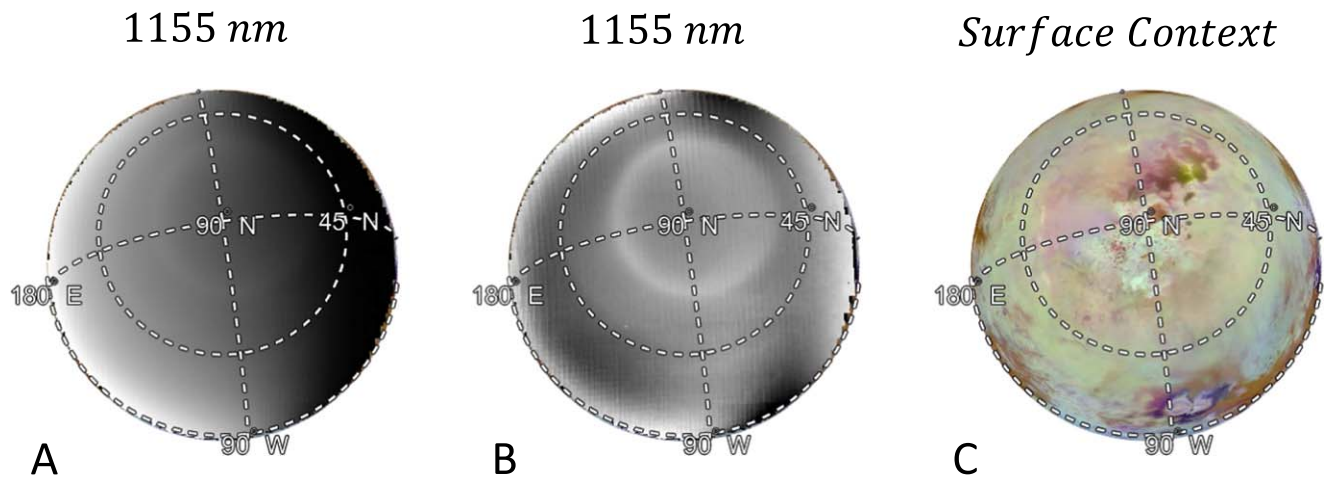
Figure 1. Orthographic mosaics of T096, 2013-12-01, $L_S = 51°2$. (A) 1155 nm mosaic. (B) 1155 nm mosaic with manifold correction. (C) Context using VIMS-ISS map (Seignovert et al. 2019).

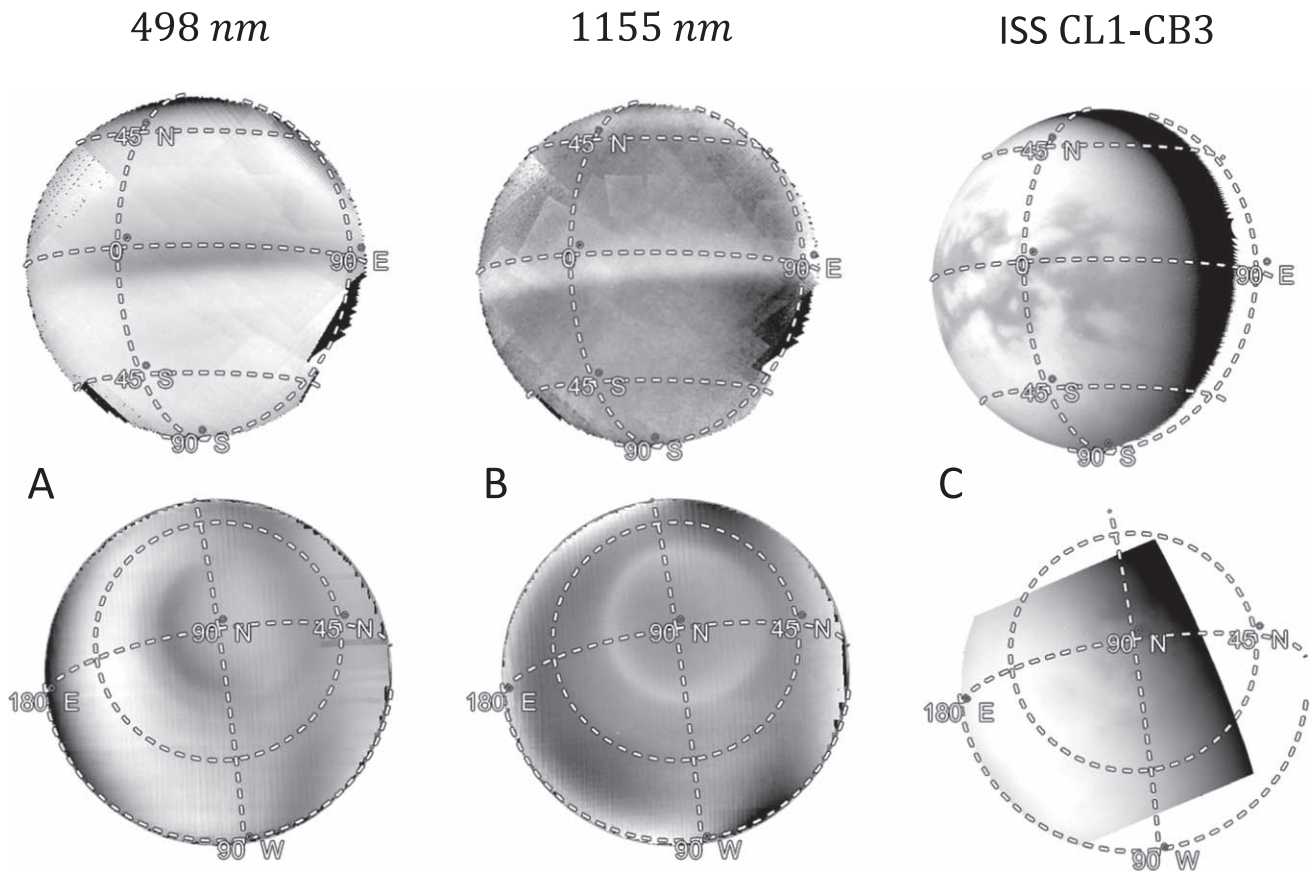**Figure 2.** Top: T061, 2009-08-25, $L_S = 0°49$; bottom: T096, 2013-12-01, $L_S = 51°2$. (A) 494 nm mosaic with manifold correction. (B) 1155 nm mosaic with manifold correction. (C) ISS NAC observations taken during the same respective flyby. Both are taken with filters CL1 and CB3 with an effective wavelength of 938.03 nm (Knowles 2016). Image names are N1630071434_1 (top) and N1764434226_1 (bottom).

meridional convergence zones and can be used to understand the pattern of zonal circulation. Annular modes of variability have recently been identified in the atmospheres of Mars and Titan (Battalio & Lora 2021a). Annular modes such as these explain much of the internal variability of Titan's troposphere as simulated in a global circulation model (GCM). The gas giants (Jupiter and Saturn) and the ice giants (Uranus and Neptune) all display patterns of planetary banding, with regions of different temperatures, composition, aerosol properties, and dynamics separated by strong meridional and vertical gradients in the zonal (i.e., east–west) winds (Fletcher et al. 2020). Auroras are particularly bright bands found on the giant planets, Earth, Mars, and Ganymede. Auroras at Ganymede reveal that the largest moon of the solar system has an internal ocean (Saur et al. 2015). Jupiter's auroras are used as evidence in explaining why the gas giant's upper atmosphere is much hotter than expected from sunlight alone. Spectroscopic observations of these bands from Keck II suggest that the
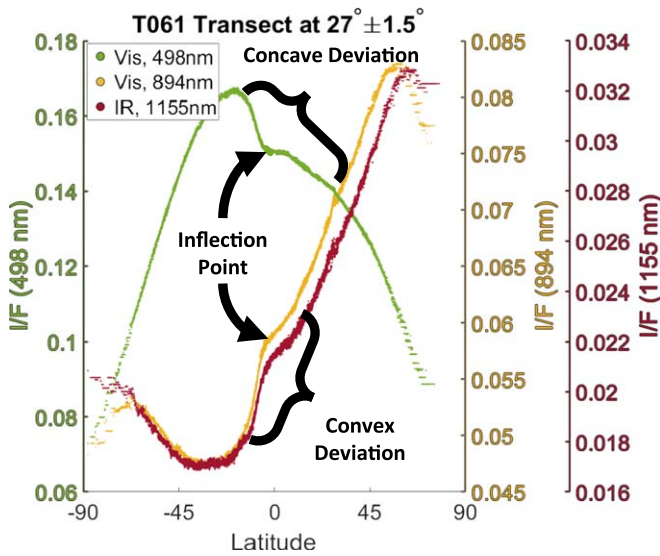
Figure 3. Transect of pixels from mosaic of T61 flyby [2009-08-25] (see Figure 2). The deviation in each of the three curves is attributed to the EQA. The inflection point of each deviation is attributed to the center of the annulus, and the Gaussian tail on either side of the inflection point is the uncertainty in locating the annulus. The north–south asymmetry appears as the smooth parabolic curve between the hemispheres. The EQA adds a sharp deviation in the curve, without which the north–south asymmetry would appear as a gradient between the hemispheres, rather than the asymmetry we see.

excess heat is produced by the redistribution of auroral energy (O'Donoghue et al. 2021).

Observations of Titan show that the stratosphere is super-rotating with wind speeds of ~ 200 m s^{-1} (Flasar & Achterberg 2009). Several Titan GCMs are able to reproduce the superrotation, though not always with wind speeds matching observations. The results of these GCMs are in agreement with the Gierasch−Rossow−Williams (GRW) mechanism for producing superrotations (Hörst 2017). In the GWR mechanism, angular momentum is transported to higher altitudes and then poleward by mean meridional circulation and is transported down and to the equator by barotropic waves generated by instabilities on the edges of the high-latitude jets (Gierasch 1975; Rossow & Williams 1979; Hourdin et al. 1995; Lebonnois et al. 2014).

Analysis of the stratospheric superrotation by the Cassini Composite Infrared Spectrometer (CIRS) revealed the strato-sphere to be tilted $4°$ with respect to the solid-body rotation axis (Achterberg et al. 2008). Multiple observations of the tilt showed that it was directed $76°$ west of the subsolar longitude. Further observations using CIRS suggest that the tilt is not fixed in a solar reference frame, but rather fixed in an inertial reference frame (Achterberg et al. 2011). The tilt has been confirmed by multiple follow-up investigations using composi-tion and tracking atmospheric features (Achterberg et al. 2008; Roman et al. 2009; Teanby et al. 2010; West et al. 2016).

While mechanisms that explain the tilt and its relationship with superrotation have been put forth (Achterberg et al. 2008; Tokano 2010), there remains a lack of consensus. Achterberg et al. (2008) proposed that the tilt, by feedback between the circulation and the heating, facilitates the vertical transport of angular momentum to balance the heat flow and insolation at low latitudes. Tokano (2010) proposed that the tilt is the result of thermal tides and is only possible if atmospheric waves perturb the circulation. With the annuli, we are able to produce

a time series set of measurements of the tilt, as well as its azimuthal offset, throughout the Cassini mission (2004–2017), which provides an important database that can be used for future modeling of the origin and evolutions of the tilt, the superrotation of the middle atmosphere, and the link between them.

Saturn's eccentricity (0.055) and obliquity (26°7) dictate the variation in the amount and location of haze production throughout a Titan year. The obliquity also causes the meridional circulation to be asymmetric about the equator and to reverse semiannually (Lebonnois et al. 2012; Teanby et al. 2012). The flow rises in the summer polar region and descends in winter polar regions. As the cells redistribute the heat in Titan's atmosphere, it also vertically transports gases and aerosols to high altitudes, transports them horizontally across the globe, and carries them back down to lower altitudes. During the fall and spring seasons, the single pole-to-pole cell splits into two symmetric cells, where the atmosphere ascends at the equator and descends at each of the poles (Mitchell et al. 2006; Tokano 2011; Newman et al. 2016; Lora et al. 2019; Battalio et al. 2022). We discuss in Section 4 the apparent correlation of the annuli presence and location with the predicted meridional circulation cell cycle.

1.1. The Equatorial Annulus

The EQA occurs at the boundary of the north–south asymmetry (Roman et al. 2009; de Kok et al. 2010). The north–south asymmetry is a feature of Titan's atmosphere where one hemisphere is darker than the other; which hemisphere is darker varies as a function of time, and the degree of contrast varies with wavelength. The north–south asymmetry was first observed in 1980-11-11 in Voyager 1 observations (and retrospectively observed in Pioneer 11 observations, 1979-08-31) and has since been observed continuously by ground-based telescopes, HST, and Cassini (Smith et al. 1981; Sromovsky et al. 1981; Caldwell et al. 1992). Previous analysis of ISS data from 2004 to 2007 indicates that the EQA/north–south asymmetry was present at around 80 km altitude with an axial tilt of $3°8 \pm 0.9$ relative to the spin axis, with the vector directed $79° \pm 24°$ to the west of the subsolar longitude (Roman et al. 2009). A height of 80 km, with possible additional contributions between 50 and 150 km, was also inferred for the EQA from Cassini VIMS (de Kok et al. 2010), while CIRS measurements of HCN indicated that the hemispheric asymmetry extended to at least 125 km (Teanby et al. 2010). In images of scattered light, the EQA helps to exaggerate the difference between the hemispheres (Figure 3). The variability in altitude estimations above can be attributed to the variety of instruments used, changes in the EQA over time, and targets accessed, i.e., the HCN used by Teanby et al. (2010) may be a part of the EQA but at an altitude different from the haze in the north–south asymmetry used by Roman et al. (2009).

The EQA is one of the few features observed at visible wavelengths that has been observed between Titan years, as the EQA can be inferred from observations of the north–south asymmetry seen by Pioneer 11 (1979 September, Tomasko & Smith 1982), Voyager 1 (1980 November, Sromovsky et al. 1981), and Voyager 2 (1981 August, Smith et al. 1982).

1.2. The North Polar Annulus

The NPA is, on average, spectrally and morphologically identical to the EQA. The spectra, size, and position of the NPA change more profoundly than the EQA, which we discuss in Section 4.2. Because more than half of the NPA can be seen in a single observation and there are multiple observations with the same illumination geometry taken close in time to one another, we are capable of triangulating the NPA (Section 2.4). We use the vector normal to the plane of the modeled ellipses to describe its tilt with respect to the rotation axis of Titan's solid body (θ_{NP}), its axial precession west of the subsolar longitude (ϕ_{Sol}), and its declinations in an inertial reference frame. Parameters of interest for the two models are shown in Table 1.

1.3. The South Polar Annulus

The SPA was not observed in the Cassini data, due to the timing of the event. The SPA appeared as a weak dark ring using HST at 336 nm (HST Wide Field and Planetary Camera filter F336W; Lorenz et al. 2001) and a bright collar using Keck II at 1158 and 1702 nm (W. M. Keck II KCAM and SCAM, filters J1158 and H1702; Roe et al. 2002) around 60° south latitude and centered on the south pole from 1999 to 2001. Lorenz et al. (2001) concluded that at least some of the material responsible for this feature must be at altitudes of above 150 km. Roe et al. (2002) used the presence of the SPA in the J1158 Keck filter to conclude that SPA must be at or above 40–50 km altitude. Both Roe et al. (2002) and Lorenz et al. (2001) note the similarity of the SPA they observed with the dark northern collar observed by Voyager 2 around the north pole and suggested that the SPA has a seasonal origin. The altitude difference between Roe et al. (2002) and Lorenz et al. (2001) can be attributed to the different wavelengths used to interpret the altitude (i.e., 336 nm versus 1702 nm).

2. Data/Methods

Our processing workflow starts with the publicly available VIMS data set on the Planetary Data System (PDS; Le Mouélic et al. 2019, https://pds-imaging.jpl.nasa.gov/data/cassini/cassini_orbiter/covims_0001/data/). VIMS consisted of two imaging spectrometers: a visual detector (VIMS-Vis) with 96 channels between 0.35 and 1.05 μm, and an infrared detector (VIMS-IR) with 256 spectroscopic channels between 0.89 and 5.13 μm (Brown et al. 2004). The absorption and scattering by methane, nitrogen, and haze mean that some channels in VIMS can see the surface, while for other channels the atmosphere is completely opaque (Corlies et al. 2021). For every pixel, we determined the viewing geometry and location information using the SPICE toolkit from NASA's Navigation and Ancillary Information Facility (Acton et al. 2018).

2.1. Data Correction and Mosaicking

We created supersampled mosaic images of Titan for ingress and egress observations of each flyby, weighting higher spatial resolution pixels more in the mosaicking. We rasterized the pixels to a spatial resolution of 5 km^2 and calculated the weighted average of all individual image pixels that filled each pixel of the mosaic. The primary constraints on data incorporated into the mosaics were a pixel scale of less than 250 km and a change in the phase angle, θ, of less than 3°. This

means that closest-approach observations, with their rapidly changing viewing geometry, were not used.

VIMS image cubes from the Vis detector have stripes of varying brightness at each sample running across the lines. The stripes are due to offsets of about 100 DN introduced by the readout electronics on the signal (Filacchione et al. 2007). We developed a destriping routine, described in Appendix A, which we applied to every VIMS-Vis image cube.

We leverage Titan's smoothly scattering atmosphere to improve contrast in the image cubes and increase spectral clarity (see Appendix B). Manifold corrections were applied to all image cubes from both detectors, although we only used the manifold-corrected data for making mosaics and examining images (Figures 1 and 2). Data used for spectral analysis, like the transects discussed below, have no corrections applied except the VIMS Radiometric Calibration, RC19 (Clark et al. 2018), which is applied to all VIMS PDS data, and the destriping applied to VIMS-Vis.

2.2. Identifying the Annuli through Transects

Taking a north–south transect of the pixels in a mosaic at a single longitude and over all latitudes produces a curve of brightness for the queried wavelengths and longitudes (Figure 3). In these meridional transects the band can be seen as a deviation in the normally smooth and featureless curves. For wavelengths where the annuli are darker than the surrounding atmosphere, the deviation is concave, while for wavelengths where the band is bright, the deviation is convex.

We used the transects to determine the presence and location of the annuli. We propose that the center of the annulus is at the inflection point for the observed deviations and that the width of the annulus is where the deviation returns to the smooth path. The annuli in general appear darkest at ~500 nm and brightest at ~1150 nm, and they are also very bright at ~900 nm. We use these three channels to investigate the annuli because they show the greatest contrast and span both the VIMS-Vis and VIMS-IR detectors. Using both detectors to identify the annuli is necessary for redundancy because occasionally one detector will have bad data. We took transects of each flyby on the ingress and egress hemisphere, every 10° of longitude (i.e., 60°, 70°, 80°, etc.) and spanning all visible latitudes. This produced a data set of 4829 transects, and each of these was examined to determine whether deviations matching the ones associated with the annuli were present.

We created a data set of annuli detections with information on the viewing geometry, coordinates, and time of observation by analyzing the transects. Transects were analyzed manually in a random order (randomizing over both flyby and longitude) to prevent unintentionally biasing our search to patterns seen when looking at consecutive longitudes in the same flyby. We then reorganized our data and displayed those detections over the appropriate flyby mosaics. With the context of the mosaics we found that our initial search results produced many false positives. These false positives were caused by several sources, including the north polar hood, the south polar vortex, observation of the limb at irregular angles, and seams between VIMS image cubes (Kelland et al. 2018; Le Mouélic et al. 2018). We identified and removed these false positives by reinvestigating each transect, this time in flyby and longitude order, as well as viewing the relevant mosaics. We further refined and expanded our detections by explicitly looking for patterns in the location of the inflection point between the
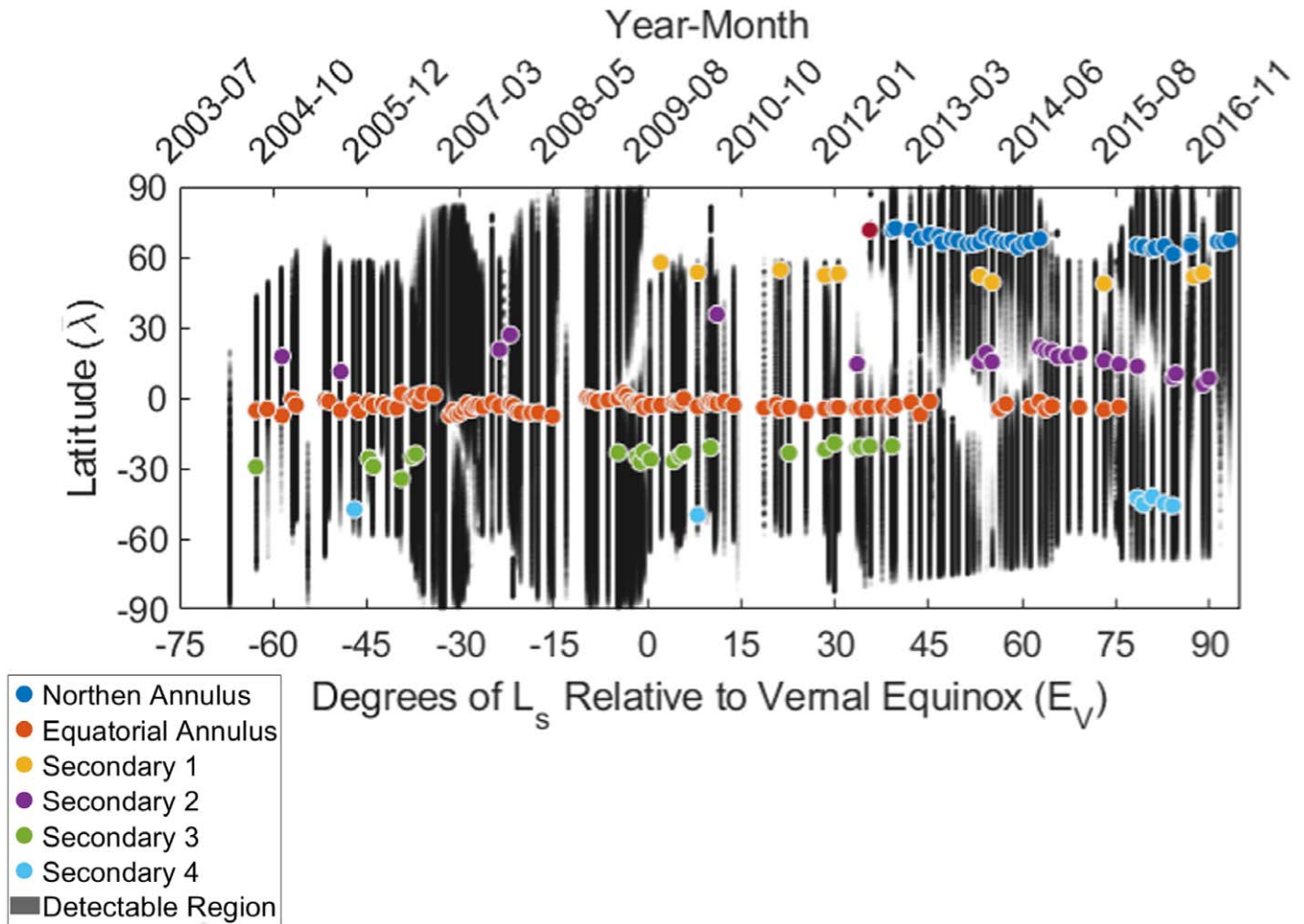
Figure 4. The average latitude of the observed primary and secondary annuli. The black regions are all the locations in time that were at a viewing geometry shared by the majority (95%) of our detections of the annuli (incidence angle $< \sim 90°$ and emission $< \sim 60°$). The red circle at $\sim 75^0$ latitude and $L_S = \sim 40°$ is a direct detection of the NPA in flyby T85.

transects that correlated to features that had the morphology of the annuli. This is the data set we use for tracking the annuli over the course of the Cassini mission and producing the sinusoidal fits and triangulated models. Our final data set contained 552 transects for the NPA and 686 transects for the EQA, as well as a total of 256 transects for the four secondary annuli. Figure 4 shows our range of detections through the average latitude of the annuli. Information on the location timing and aspects, such as tilt of the averages of our transects, is provided in Table 1.

We use the transects to acquire spectra of the annuli. The spectrum of the annuli has no distinguishing features when compared to spectra taken from pixels located just north or south of the annuli (Figure C). This suggests that the annulus is compositionally indistinct from the rest of the atmosphere and that observed brightness differences are the result of a local increase in haze optical depth. Instead of a typical VIMS spectrum, we investigated the differential spectrum of the annuli, $\Delta I/F$. Using the transects, we identify the northern and southern edge of the annuli, i.e., where the smooth featureless atmosphere transitions to the deviation of the annuli and back again. We use these bounds to remove the deviation from the curve, and we then interpolate the data spanning the resulting hole. We use a straight line (first-degree polynomial) to interpolate the data. We have investigated using a second- and

third-degree polynomial, as well as splines, and the results are very similar. We therefore use the straight line, as anything more complicated is not justifiable. The differential spectrum is then the maximum difference between the deviation and the interpolated data. Figure 5 shows the average differential spectrum of the T061 EQA. This is a good representative of the EQA and NPA spectra, except for early and late spectra of the NPA, which we discuss in Section 4.2.

2.3. Altitude from Spectra/Spectraltimetry

We estimated the altitude of the annuli using spectraltimetry. Features entrained in an absorbing medium will become visible at different pressure levels dependent on the wavelengths. Using superposition, we can infer the shape and altitude/depth of a feature by its appearance in the spectra. This technique has already been used extensively at Titan for measuring the height of clouds using observations from Cassini and ground-based telescopes (Brown et al. 2002; Le Mouélic et al. 2012; Ádámkovics et al. 2016; Corlies et al. 2021). As methane is the primary absorber in Titan's atmosphere at IR wavelengths, we used a methane opacity profile from Rannou et al. (2016) to estimate the altitude of the EQA and the NPA. We calculated the altitude where the atmosphere becomes opaque in two ways. First, we determined the altitude, H, where the sum of the weighted (with Gauss coefficients) effective optical depth
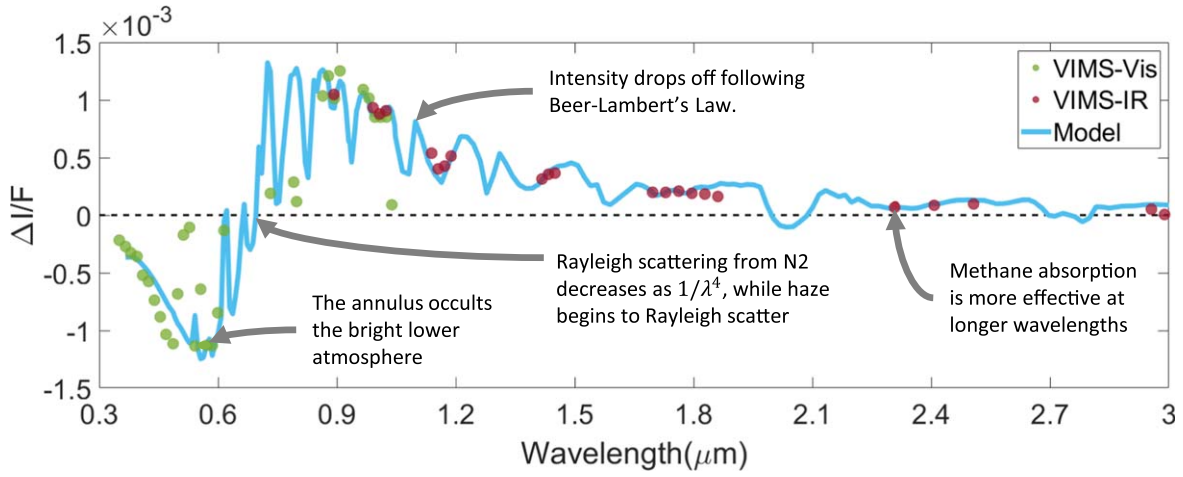
Figure 5. Averaged differential spectrum of the EQA from $L_S = 345°$ to $15°$ (flybys T044–T072). The differential spectra shown with the cyan curve are produced from the difference between model spectra with typical haze abundance and model spectra where the haze abundance is increased at 100–130 km by 10%.
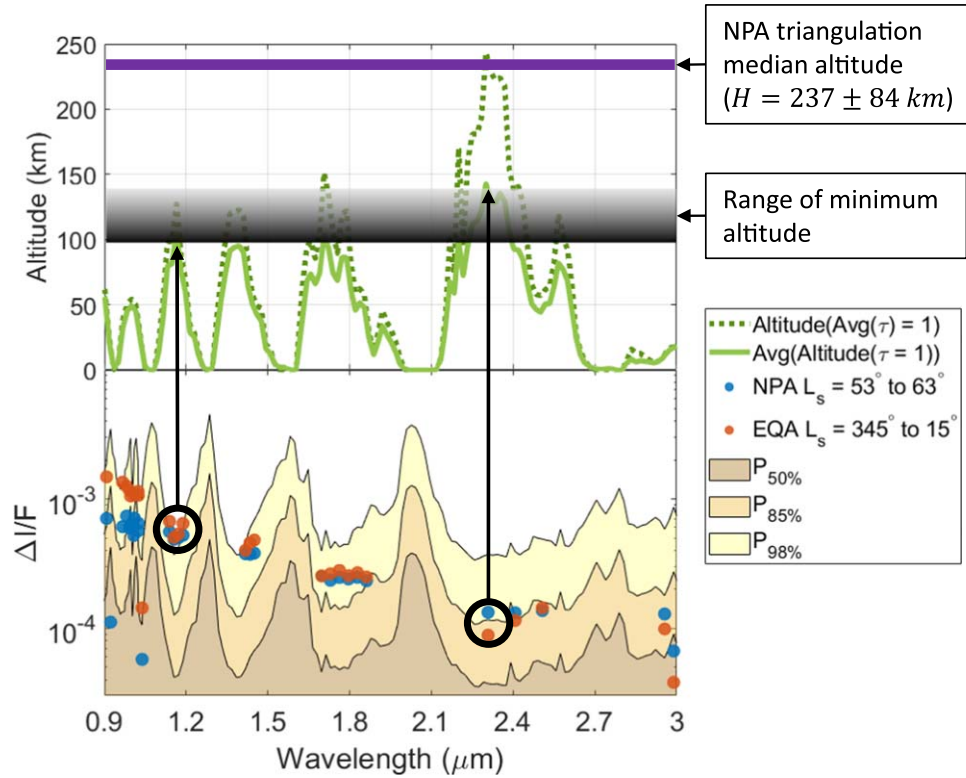

Figure 6. The averaged differential spectra of the NPA (blue) and the EQA (orange) from $L_S = 55°$ to $65°$ and from $L_S = 345°$ to $15°$, respectively. The purple line indicates the average median altitude of Model A and Model B from our triangulation efforts of the NPA (Section 2.4). The green curves show the modeled altitudes where the atmosphere is opaque when averaged over the different terms of the k-correlated description. Solid green curve: the altitudes where the average column opacity is equal to 1. Dashed green curve: the average altitude where the column opacity is 1. Yellow, gold, and brown are the 50th, 85th, and 98th percentile values of the difference between neighboring pixels across all flybys, respectively. Features in the differential spectra are significant if they are outside these bounds. The gray area shows the range of expected minimum altitudes based on the detection at ~1.2 μm with $> P_{98\%}$ and the detection at ~2.3 μm with $\approx P_{85\%}$.

(following Pollack & McKay 1985) calculated with four k-correlated coefficients where $\tau(z) = \sum_{i=1}^{4} w_i \tau_i(z)$ is equal to 1 (Goody et al. 1989); this is the dotted green curve in Figure 6. Second, we determined the average H as the weighted altitude (with Gauss coefficients) $H = \sum_{i=1}^{4} w_i H_i$ calculated from the altitudes H_i where the effective $\tau_i(z)$ are equal to 1; this is the solid green curve in Figure 6. We believe that the second method is more appropriate for spectraltimetry.

In order to determine the altitude of a feature, we must first determine whether the difference of the feature from the rest of the observation is significant. To determine the significance of a feature, we used a similar approach outlined in McCord et al. (2008 and references therein). We found the $\Delta I/F$ between neighboring pixels in our mosaics and determined their nth percentile values, $P_{n\%}$. We found that our 125 mosaics all had similar $P_{n\%}$ values, and so we opted to use the average across all
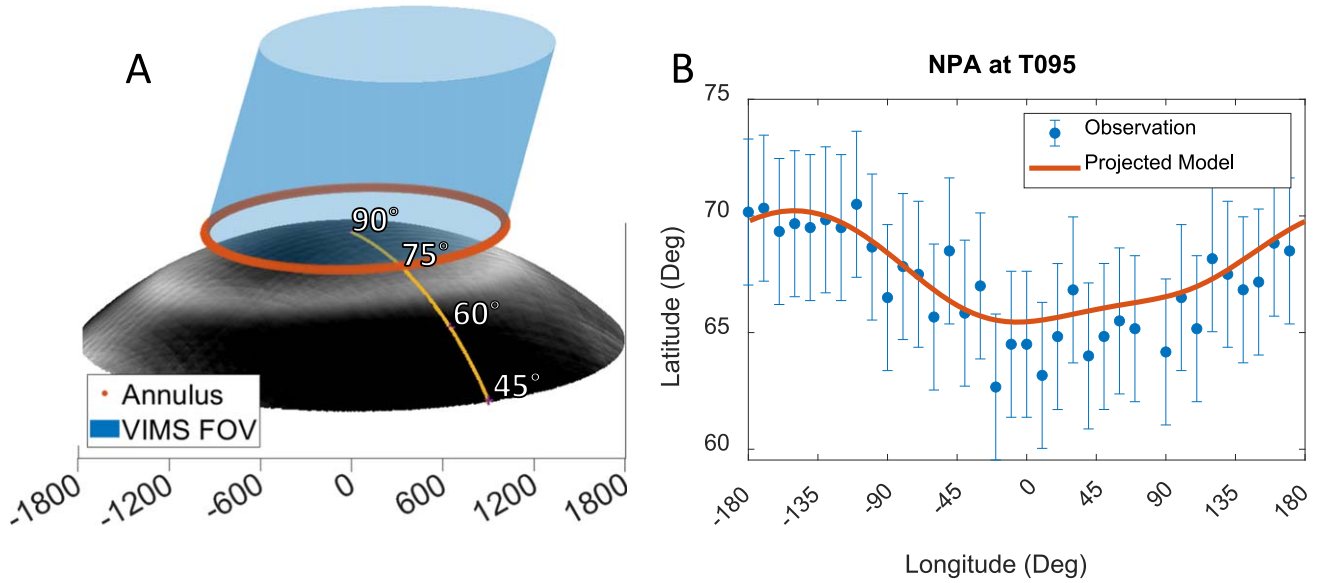
Figure 7. T095, 2013-10-14, $L_S = 49°.7$. (A) Our triangulated model of the NPA (orange) and the contemporaneous VIMS observation (black and white) projected onto Titan as seen from the side. (B) The projection of the modeled annulus onto Titan (orange) fitting our observation of the annulus (blue) in Lat–Lon space.

mosaics, $\bar{P}_{n\%}$. We suggest that a feature i is significant (meaning that its $\Delta I/F$ is outside the range of $\Delta I/F$ between neighboring pixels that come about via noise) if $\Delta I/F(i) > \bar{P}_{98\%}(\Delta I/F)$. A feature with $\Delta I/F(i) > \bar{P}_{85\%}(\Delta I/F)$ is considered to be a positive detection as well, but it is considered with scrutiny. We chose $\bar{P}_{85\%}$ and $\bar{P}_{98\%}$, as these percentiles represent a statistical significance similar to 1σ and 2σ, respectively, for normal and nonnormal distributions. As can be seen in Figure 6, the differential spectra of the annuli are significant from the background up to the methane absorption channels at around $\sim 1.4\,\mu m$. At these wavelengths Titan is essentially opaque, at ~ 100 km. At the next series of absorption channels at around $2.4\,\mu m$, the differential brightness falls within $\bar{P}_{85\%}$, suggesting an upper limit of the minimum height of ~ 130 km. Regardless of how bright annuli are at other wavelengths, they all fail our criteria beyond $2.6\,\mu m$. In images of the annulus at these wavelengths, it is very difficult to discern the annulus from the rest of the atmosphere. By $3.0\,\mu m$ it becomes difficult to interpret the spectraltimetry. We suggest that this is not due to the annulus being below a certain opaque altitude, but rather because of the low signal-to-noise ratio at these wavelengths due to lack of solar illumination and because the scattering intensity has diminished following Beer–Lambert's law. Titan's stratosphere is between ~ 50 and ~ 300 km, while the main haze layer is between ~ 100 and $\sim 400/500$ km (Hörst 2017). Depending on the flyby, the differential spectrum of the NPA is identical to the EQA, and so we can conclude that it is at the same altitude for part of a Titan year. In Section 4.2, we will discuss the altitude implications of the change in differential spectra of the NPA.

2.4. Altitude from Triangulation

We triangulate the location of the NPA by finding the intersection between multiple observations of the annulus at different times with similar illumination geometries. We produced two models where the opposite hemisphere was illuminated between the two groups. The first used observations from flybys T092–T096 ($L_S = 46°.71$ to $L_S = 51°.2$), and the second used observations from flybys T103–T107 ($L_S = 58°.37$ to $L_S = 62°.79$). These produced modeled annuli,

which we refer to as Model A and Model B, respectively. The characteristics of each model are shown in Table 1.

The true/physical location of the annuli exists along a cone connecting the observations of the annuli with Cassini (Figure 7(A)). We used the location of the inflection points on the transects to define one point on a vector extending from the position of Cassini at the time of observations of the transect to and through the annulus. We interpolated between the inflection points using a sinusoidal fit. This produced a higher-density vector field to find intersections between cones. The width of the deviation of the transects and the longitudinal bin width of the transects produce uncertainty in the location of the center of the annuli. To compensate for this, we performed a Monte Carlo simulation with 75 runs, where we randomly varied the location of our interpolated points by half of the average latitudinal width of all transect deviations ($3°$) and by the longitudinal separation between interpolated points ($2°$). In each run of the Monte Carlo simulation, we found the closest point between any and all two vectors from multiple flybys in a longitude bin with a width of $2°$.

For each flyby where we detected the NPA, we projected our modeled annuli onto Titan from the perspective of Cassini (Figure 7(B)). We then used the χ^2 goodness-of-fit statistic to determine how well our model matched our observations. The χ^2 goodness-of-fit statistic is given by

$$\chi^2 = \sum_{i=1}^{N} \frac{(\phi_i - F(\lambda_i))^2}{\sigma^2}, \qquad (1)$$

where ϕ is the latitude of the projected annuli, λ is longitude of the projected annuli, F is the function for the expected latitude, and σ^2 is the variance related to the measurement error for ϕ. As we expected, we saw a lower goodness of fit to our observations the farther in time a flyby was from either Model A's group (T092–T096) or Model B's group (T103–T107), suggesting that the annulus changes over time. We used a grid search, to investigate what changes were necessary in order to match the annulus we predicted with our observations. We varied several parameters, including tilt and altitude, but most of these could be neglected.
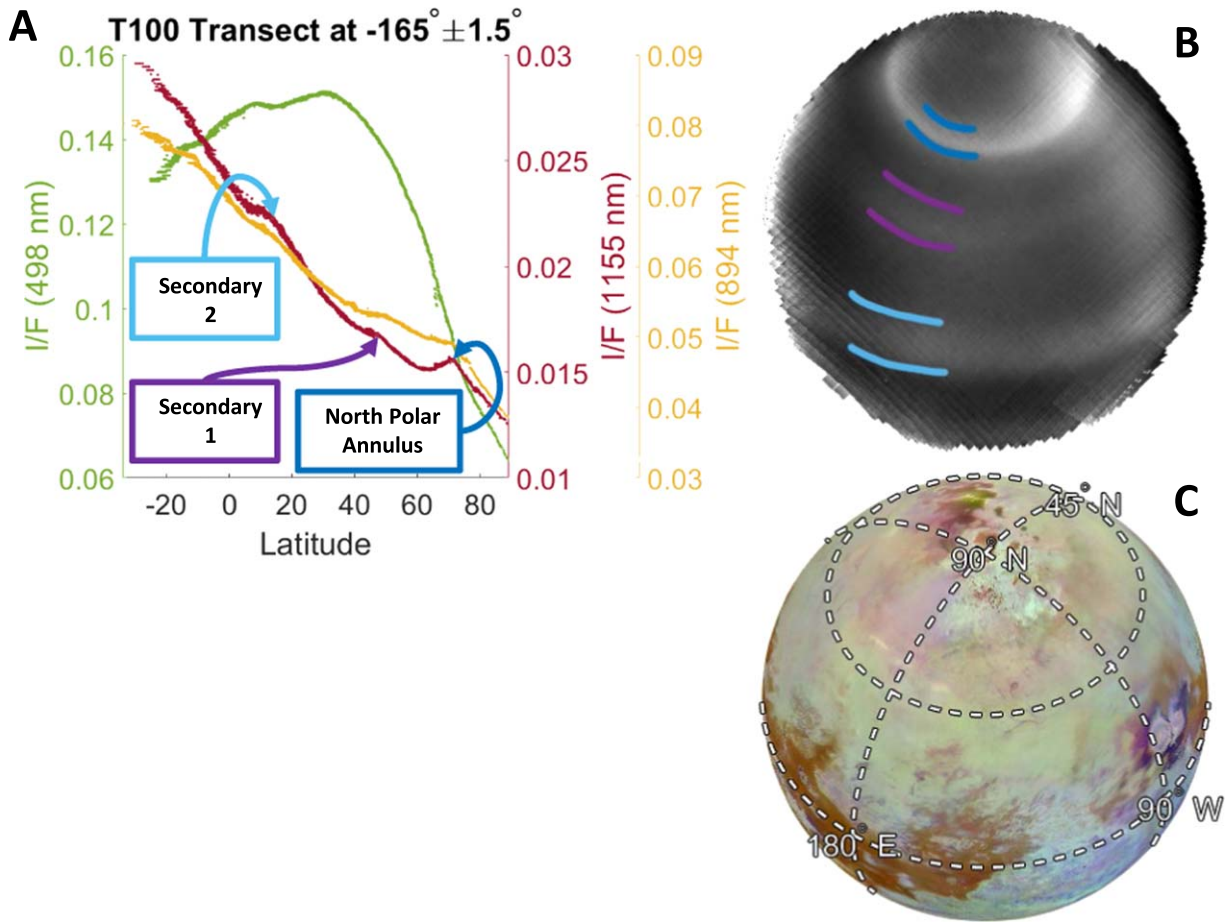
Figure 8. (A) Latitudinal transect of the mosaic for the T100 flyby [2014-04-07, $L_S = 55°17$]. One primary (the NPA) and two secondaries are shown. The nomenclature is consistent with Figure 7. The annuli are highlighted at 1155 nm, where a deviation in the otherwise smooth curve is found. Similar convex deviations are found in the 894 nm transect, and concave deviations are found in the 498 nm transect. (B) 1155 nm mosaic with manifold correction. The colored lines identify the annuli and are consistent with panel (A). (C) Context using VIMS-ISS map (Seignovert et al. 2019).

The two significant parameters we varied were the radius of the ellipse (preserving the eccentricity) from -250 to $+250$ km and the direction of the annulus's normal vector with respect to the subsolar longitude from $-180°$ to $+180°$. Changing the radius of the annulus also changed the altitude.

3. Results and Seasonality

The annuli appear roughly sinusoidal in latitude–longitude space (Figure 7), and, similar to Roman et al. (2009), we use a sinusoidal fit to determine the tilt with respect to the rotation axis of Titan's solid body (θ_{NP}), the axial precession west of the subsolar longitude (ϕ_{Sol}), and the average latitude ($\bar{\lambda}$). The average values from our sinusoidal fit coefficients (with 95% confidence bounds) to the EQA over all our observations are $\theta_{NP} = 2°78 \pm 1°63$, $\phi_{Sol} = 110°27 \pm 54°$, and $\bar{\lambda} = -3°13 \pm 2°09$. The average values for the sinusoidal fit coefficients of the NPA (with 95% confidence bounds) over all our observations are $\theta = 2°05 \pm 1°27$; $\phi_{Sol} = 162°38 \pm 85°83$, and $\bar{\lambda} = 66°39 \pm 2°01$. Our results for determining the altitude of the EQA and the NPA suggest that the annuli are at least 100 km in altitude, which puts our findings in line with Lorenz et al. (2001).

3.1. Secondary Annuli

We found four secondary annuli (Figure 8). We have grouped them together based on common latitude ranges (Figure 4). These features are nearly identical to the primary annuli spectrally and morphologically, the difference being that they are less intense and distinct. Secondary annuli 2 and 3 (using the nomenclature from Figure 4) occur within $30°$ of the equator, and sometimes both secondary annuli and the equatorial annuli can be seen together. Secondary annuli 1 and 4 occur at roughly $55°$ north and $55°$ south, respectively. It is interesting that we see the southern secondary annuli so low in latitude, while not observing the SPA. It is possible that the secondary annuli have less of a seasonal dependence in a similar way to the EQA while the SPA and the NPA are seasonal features. The secondary annuli are more sporadic than the primary annuli. This could be due to a more sensitive viewing geometry requirement. Alternatively, it may indicate that the increase in haze is especially low and that the variation in abundance can vary enough to make the secondary annuli detectable or not between observations.

3.2. When Do We See the Annuli?

In Figure 4, we plot the location of the mean latitude against the time of the observation in units of degrees of planetocentric longitude of the Sun relative to vernal equinox, L_S. The observations of the annuli are grouped largely by their mean latitude and perception of repeat observations. We found that the presence of the annuli is not correlated with the presence of tropospheric clouds, as can be seen in Figure 2(c).

The annuli are seen over a wide range of viewing geometries. But a closer inspection of each observation reveals that the vast majority (95%) occur at incidence angles, i, between 9° and 91° and at emission angles, e, between ∼4° and ∼57°. We mapped where VIMS observed Titan within these ranges, suggesting that if an annulus was in the area when these observations were taken, there would be a higher probability of detection. In Figure 4 gaps in the detection of the annuli, in particular the EQA starting at $L_S = 45°.21$ and the NPA starting at $L_S = 63°.77$, correlate well to the areas we suggest would not show an annulus, whether it is present or not.

We see the EQA during the entirety of the Cassini mission and secondary annuli for essentially the same length of time. Our earliest observation of the NPA comes from flyby T085 [2012-07-24, $L_S = 35°.61$], where the annulus can be seen as a solitary arc extending off the disk of Titan (Figure 4, red dot), and we first see the NPA as the band on the disk of Titan in flyby T087, [2012-11-13, $L_S = 39°.16$]. This is the same time that Cassini begins its inclined series of orbits to focus on Titan's north polar region. It is therefore difficult to determine whether the NPA is a seasonal feature brought about by the increase in insolation or is always present and we simply lacked the ability to observe it. The absence of the SPA gives us a clue in breaking the degeneracy, leading to our preferred hypothesis that the NPA is a seasonal feature.

We know that the SPA was observed prior to Cassini's arrival. Yet despite the existence of south polar observations with good resolution and good viewing geometry (e.g., $-32°.1–0°L_S$ relative to vernal equinox), we did not observe the SPA. From this we conclude that the SPA is absent owing to the changes in season. It was predicted by Roe (2012) that the SPA would vanish as summer moved toward fall in the southern hemisphere. Titan's stratosphere has already been shown to be periodic as the north–south asymmetry switches between either hemisphere being bright or dark. We propose that the NPA is similarly periodically symmetric to the SPA. Since the SPA is seasonal, and we also see the NPA change with the seasons as discussed below, we propose that the NPA appears according to the season. We suggest that if the NPA was present before our earliest detections, it was not significantly earlier on a seasonal timescale.

If we assume that the SPA has a similar seasonal timescale to the NPA, and given our detection of the NPA range from 2012-07-24 to 2017-09-11 ($L_S = 39°.17–93°.3$), then we could expect the SPA to be present as early as 1998 January and as late as 2003 March ($L_s ≈ 220°–280°$). If we continue to extrapolate, we should expect to see the SPA again starting around 2027 February. If, however, Earth-based observations of Titan are taken before 2027 and the SPA is observed, this would imply that the NPA should have been visible as early as 2006 December ($L_S = 315°.29$), or Cassini flyby T021. As this is not the case, an observation of the SPA before 2027 would imply that the southern stratosphere does not mirror the northern stratosphere. This might be unsurprising, as asymmetries are already observed between the atmospheres of the north/south hemispheres, such as the lag in the expected onset of methane clouds in the north following equinox (Rodriguez et al. 2009, 2011; Turtle et al. 2018).

3.3. Changes during Cassini

The differential spectra of the EQA and NPA change as the season progresses (Figures 9 and 10). The shape of the differential spectrum of the EQA remains the same as evidenced by the positions of the peak brightness and darkness
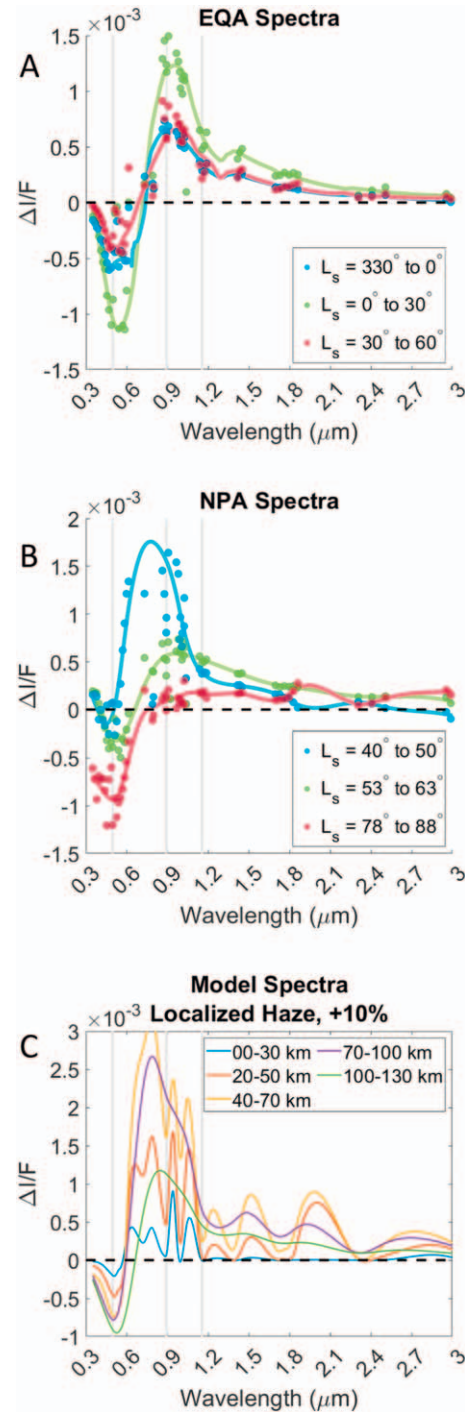
Figure 9. The colored solid lines in each figure are spline fits to the corresponding data with an $R^2 ≈ 0.95$. These curves are nonphysical and are intended to facilitate comprehension. The three vertical gray bars in each figure are located at 498, 894, and 1155 nm. These are the wavelengths used for our transects and mosaics. (A) The EQA differential spectra taken from three time periods of equal length centered about $L_S = 15°$ (the peak of the blue sinusoid in Figure 10(A)); blue is from flybys T028–T061, green from T061–T082, and red from T082–T105. (B) The NPA differential spectra taken from three time periods of equal length spanning the range of observable flybys; blue is from T088–T095, green from T098–T108, and red from T119–nT262. (C) Differential spectra produced by creating a modeled spectra where the haze abundance at a range of altitudes is increased by 10% and then subtracting a modeled spectrum with typical haze abundance.

in Figure 9(A). The amplitude, however, changes a great deal and has a very symmetric pattern, with the peak amplitude centered about 10° after the vernal equinox (Figure 11(A)). The
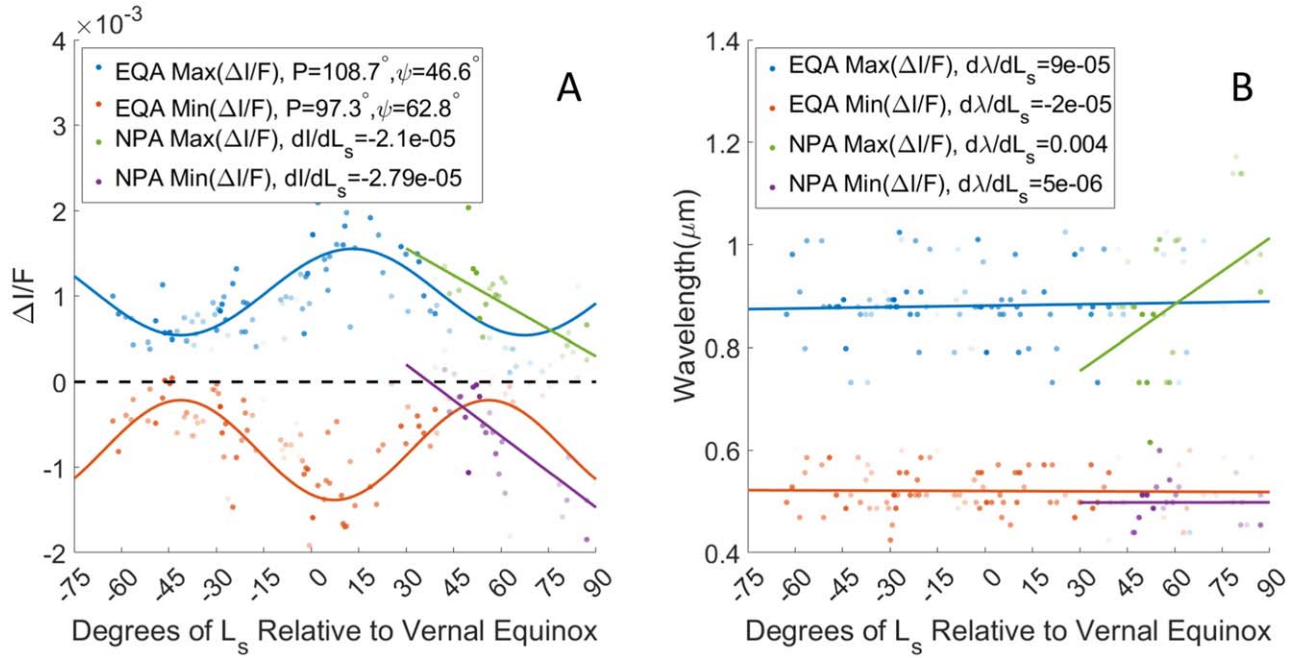
Figure 10. (A) Blue: maximum value of $\Delta I/F$ of the EQA differential spectrum. Orange: minimum value of $\Delta I/F$ of the EQA differential spectrum. Green: maximum value of $\Delta I/F$ of the NPA differential spectrum. Purple: minimum value of $\Delta I/F$ of the NPA differential spectrum. (B) Blue: the wavelength of the maximum $\Delta I/F$ of the EQA differential spectrum. Orange: the wavelength of the minimum $\Delta I/F$ of the EQA differential spectrum. Green: the wavelength of the maximum $\Delta I/F$ of the NPA differential spectrum. Purple: the wavelength of the minimum $\Delta I/F$ of the NPA differential spectrum. The opacity of the data points correlates to the relative weight of the data. Data are weighted according to the number of transect detections. For details on the curves, see Table 2.
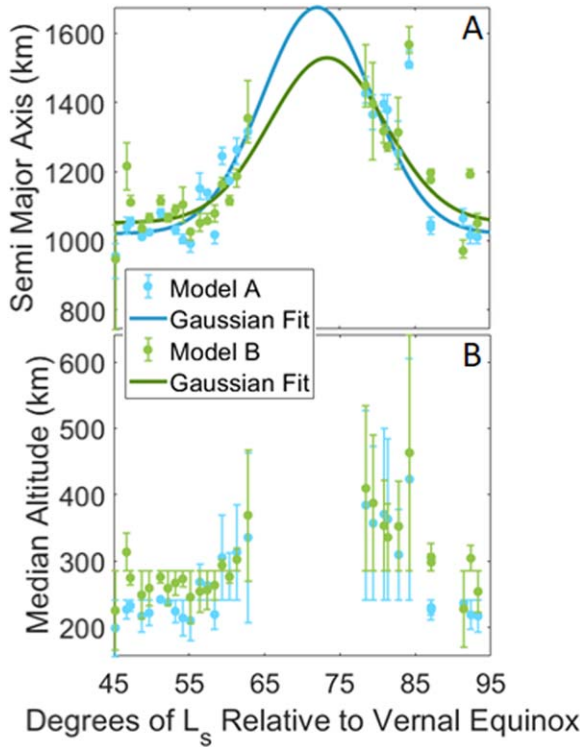
Figure 11. Both panels show the results of the χ^2 minimization routine to determine the change in parameters of the NPA. Model A was constructed using flybys T094–T098, and Model B was constructed with flybys T101–T105. (A) Semimajor axis of the NPA as a function of L_S. The curves are Gaussian fits, with (B) median altitude of the NPA vs. L_S. The change in altitude is a product of the change in semimajor axis.

nature of the spectral changes for the NPA is different from that of the EQA. The entire spectrum of the NPA becomes darker as we approach summer solstice. The bright part of the spectrum moves redward, while the dark component shows a small shift to bluer wavelengths (Figures 9(B) and 10(B)).

Our triangulated models indicate that the semimajor axis of the NPA increases as Titan approaches northern summer, potentially reaching a maximum size of about 1500 km around $L_S = 72°$ (Figure 11(A)). This may be due to the meridional circulation transporting the haze that had been lofted by the onset of the pole-to-pole circulation cell, toward the south pole. As the annulus increases in radius, it also increases in altitude, assuming a constant tilt (Figure 11(B)). This may imply that the change in altitude we suggest based on the changing spectra of the NPA is caused by the NPA increasing in size, rather than the NPA being lofted higher itself. After $L_S = 72°$, the size of the annulus seems to decrease, returning to its original size just before summer solstice.

3.4. The Tilted Pole

In a review of open questions at Titan following Cassini, Nixon et al. (2018) ask, "*Is the* [azimuthal and tilt offset of the stratosphere] *fixed in magnitude and direction, or does it wander on seasonal or longer timescales*?" In Figures 12, 13, and 14 we show the change in the tilt and the offset as a function of time in solar and inertial reference frames. We note that the data for the EQA and NPA are contiguous but not continuous; however, where appropriate we analyzed and interpreted the data as if they were one continuous set.

Achterberg et al. (2011) suggested that a longer time base of stratospheric tilt offset may reveal the offset to be fixed in an
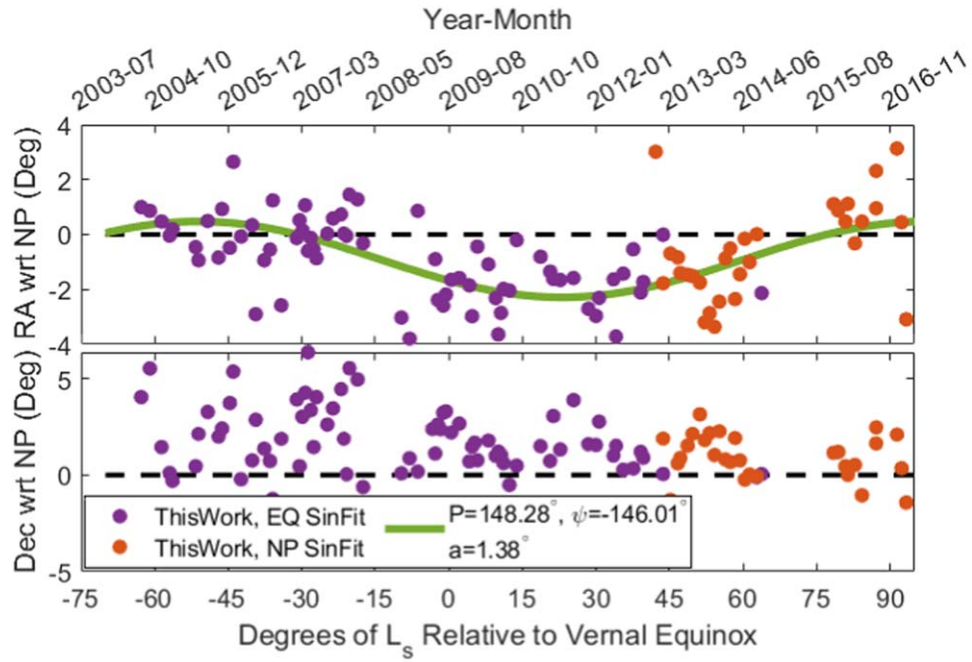
Figure 12. Top: the R.A. offset of the normal vector of the annuli from the solid-body rotation axis in an inertial reference frame (ICRF). The R.A. of Titan's solid-body rotation axis is R. A. = 39°.48 (Stiles et al. 2008). The green sinusoid through the flyby has a goodness-of-fit metric of $R^2 = 0.411$. Bottom: the decl. offset of the normal vector of the annuli from the solid-body rotation axis in an inertial reference frame (ICRF). The decl. of Titan's solid-body rotation axis is R.A. = 83°.43 (Stiles et al. 2008).

Figure 13. Top: western azimuthal offset of the normal vector of the annulus from the subsolar vector. The yellow squares are taken from Roman et al. (2009), Table 1, Column (6). The black crosses are taken from Tokano (2010), Figure 6(b). Bottom: magnitude of the polar offset of the normal vector of the annulus from the solid-body rotation axis (north pole). The red line is taken from Tokano (2010), Figure 5(a).
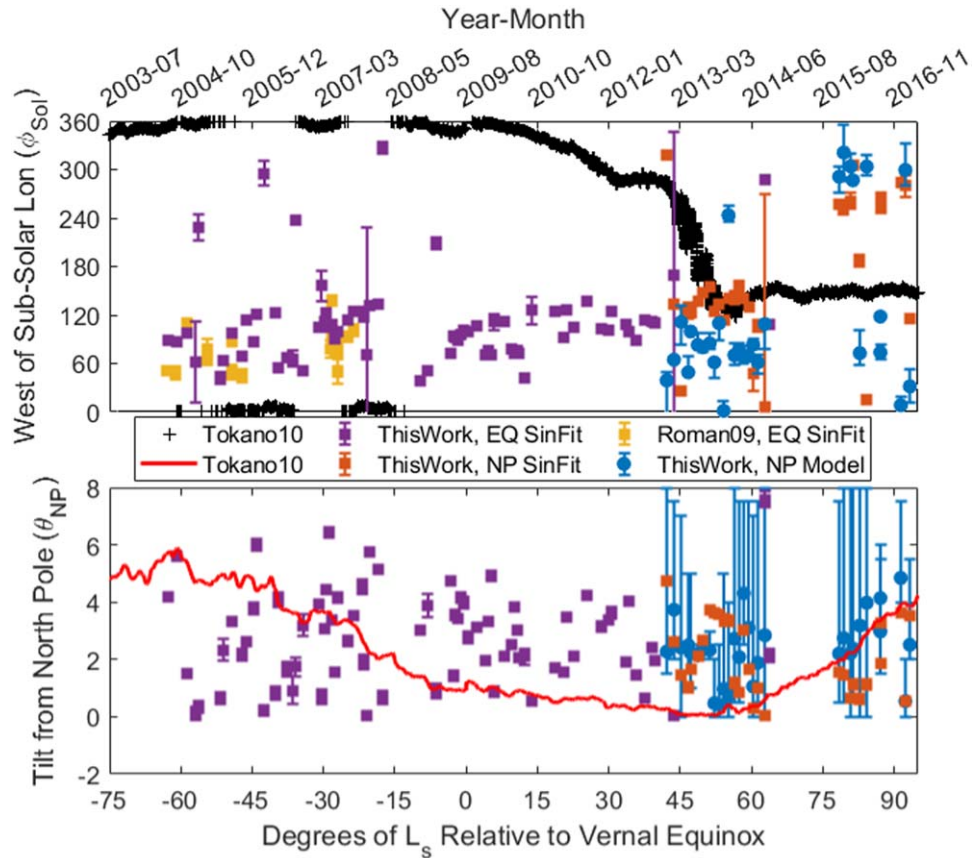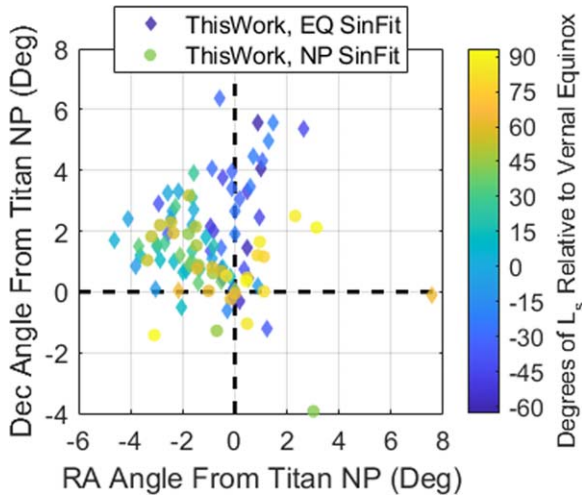
Figure 14. The R.A. and the decl. offset of the normal vector of the annuli from the solid-body rotation axis. Diamonds are data from the EQA, and circles are data from the NPA. The colors correspond to the time of observation.

inertial (star-fixed) reference frame. We determined the R.A. and decl. difference between the normal vector of the annulus and the Titan solid-body rotation axis (Stiles et al. 2008) aligned to the *X*-axis of the International Celestial Reference Frame (ICRF; Charlot et al. 2020). In Figure 12, we see that, instead of being fixed, it appears that the stratospheric tilt offset in an inertial frame is a function of the Titan season. We modeled the oscillation of the R.A. of the stratosphere about the north pole ϕ_{NPRA}, as a function of L_S,

$$\phi_{\mathrm{NPRA}}(L_s) = \phi + M \sin\left(\left(360\frac{L_s}{P} + \psi\right)\frac{2\pi}{360}\right), \qquad (2)$$

where ϕ is an offset in R.A. of the north pole of Titan, M is the amplitude, P is the period, and ψ is the phase shift. We used the bisquare weights method to minimize the influence of outliers. We found that the coefficients (with 95th percentile bounds) for the EQA and NPA combined are $\phi = -0°.9071 \pm 0°.38$, $M = 1°.38 \pm 0°.35$, $P = 148°.3 \pm 36°.3$, and $\psi = -146° \pm 18°.5$. The curve in Figure 12 fits our data with an $R^2 = 0.411$.

Additionally, we find that the tilt offset in a solar reference frame (i.e., the subsolar longitude) is also a function of the season (Figure 13). We assume that the stratosphere is a triaxial ellipsoid, although hemispheric asymmetries of the atmospheric angular momentum (AAM) are possible and perhaps necessary to explain our observations (Tokano 2010). Since each group can be characterized by a first-degree polynomial and considering both would require a more complicated model, for now we will describe their progression separately. We find that the EQA rotation axis precesses westward at a rate $d\phi_{\mathrm{Sol}}/dt = 0.21 \pm .23(+W°/L_S)$, with a starting point at vernal equinox $\phi_{\mathrm{Sol}}(0) = 99°.22 \pm 7°.51$. We find that the NPA rotation axis precesses westward at a rate $d\phi_{\mathrm{Sol}}/dt = 3.85 \pm .99(+W°/L_S)$, with a starting point at vernal equinox $\phi_{\mathrm{Sol}}(0) = -71°.3 \pm 66°.41$. This contradicts the prediction from Tokano (2010) showing a time series of the angular distance from the subsolar longitude that moves eastward as the season progresses (Figure 13).

Tokano (2010) explains the movement of the equatorial AAM as a result of the seasonal reversal of the meridional circulation. The reversal of the meridional circulation cell causes a simultaneous change in the components AAMx and AAMy, which manifests itself as a $180°$ shift of the tilt. Tokano (2010) did not emphasize that AAMx and AAMy also depend on the zonal wind u. If u is very large (as is the case in Titan's stratosphere), a sign change of v may have little influence on AAMx and AAMy according to Equations (1) and (2) of Tokano (2010). From a comparison with Achterberg et al. (2008), the zonal wind in the stratosphere produced by Tokano's GCM is too weak, and this could bias the seasonal variation in the AAM tilt angle. It is probable that the weight of v of the equatorial AAM is too large relative to that of u. An additional reason may be an underestimation of the axial component of AAM, AAMz, in the calculation of the tilt angle by Tokano (2010). According to Tokano & Neubauer (2005), AAMz strongly varies with season owing to seasonal reversal of the zonal wind direction in the lower troposphere. However, since the stratospheric superrotation in their GCM is greatly underestimated, it is likely that the seasonal variation in AAMz relative to the annual-mean AAMz is too large. In reality, the mean AAMz may be much larger, while its seasonal variation due to tropospheric winds remains unchanged. This implies that the lack of a systematic seasonal tilt angle of the stratosphere in the observational data is evidence of the relative seasonal invariance of the axial AAM due to perennial stratospheric superrotation. Our results, however, do seem to match Tokano's (2010) predictions for the NPA between $40°$ and $60°$ past the vernal equinox. This might indicate that the GCM from Tokano (2010) could predict the rotation of the stratosphere by using observations such as those presented in this work to further constrain the model.

Tokano (2010) shows in his Figure 4 that the tilt of the stratosphere with respect to the north pole should vary from $0°$ to $8°$ biannually, with the maximum tilt peaking around $30°$ of planetocentric longitude of the Sun after summer and winter solstice. We find that the tilts of the EPA and NPA stay within the bounds predicted by Tokano (2010), but with much greater variability (Figure 13). We found a weak correlation between the variability and differences in the longitudinal extent of some of our observations, which may indicate inaccuracies in our tilt estimations. The upper limit of our tilt measurements follows the same path predicted by Tokano (2010), decreasing at the same rate between $-60°$ and $65°$ relative to the vernal equinox. That the rate of change predicted by Tokano (2010) is consistent with what was observed over the Cassini mission indicates that the forces that change the tilt were accurately modeled.

4. Discussion

We propose that the annuli are features of enhanced aerosols that are corralled/confined by gradients in the winds, or at least mark locations where aerosols are in a stable quasi-equilibrium for an extended time period. Given their location, circumglobal nature, and seasonal behavior, we suggest that the annuli are caused by the meridional cell circulations, with different mechanisms for the NPA and EQA, respectively.

4.1. Detailed Explanation of the Spectra

4.1.1. 300–500 nm

The difference spectrum is negative for wavelengths shorter than ~ 700 nm, indicating that the annuli are darker than the surrounding atmosphere (Figure 5). The local darkening could

be produced by multiple scattering in a higher optical depth environment removing net-outbound photons, or by absorption of inbound photons that never get a chance to scatter from the low-altitude gases. Rayleigh scattering is the dominant mechanism of scattering by particles much smaller than the wavelength of light ($x = 2\pi r/\lambda \ll 1$, for particles of radius r and wavelength λ) and has an intensity dependence of $I \propto 1/\lambda^4$. In the lower atmosphere scattering by gaseous nitrogen and methane dominates; since both have a kinetic radius of $r \approx 0.2$ nm, the lower atmosphere is highly back-scattering. The annuli, however, if predominantly made of haze particles, will have effective radii around 1.0–2.0 μm (Lavvas et al. 2010), which leads to aerosol/particle scattering at these wavelengths with only a small backscatter component (in the limit of spherical particles this is Mie scattering). Outbound photons scattered by the gases that interact with the annuli must contend with a higher optical depth, which is not encountered outside the annuli. Alternatively, the haze or a companion species may have absorption features around 500 nm. In this scenario photons are absorbed more effectively in the higher optical depth environment of the annuli, producing the contrast we observe.

To test this hypothesis, we use a model that predicts the photometry in UV and visible (e.g., Rannou et al. 2016). This model is tuned to fit Titan's spectra near the equator, as observed in a near-nadir viewing (e.g., spectra from VIMS observation CM_1477457253_1 in flyby TA). We then successively increase by 10% the haze opacity in different layers in order to assess the effect of this change on the outgoing intensity relative to the reference model, producing a modeled differential spectrum. As can be seen in Figure 5, an increase of 10% haze opacity at 100–130 km produces differential spectra nearly identical to the averaged differential spectra of the EQA from 345° to 15° L_S. A more complete radiative transfer model is needed to determine whether the mechanism of obscuration only arises from an increase in haze opacity at a specific altitude or changes in scattering and absorption properties are also needed to explain the data in fine detail.

4.1.2. 500–700 nm

Beginning with 500 nm and progressing redward, the brightness of the annulus starts to increase (Figure 5). Nitrogen and methane move further into the Rayleigh scattering regime, but the intensity from the lower atmosphere, optically thick because of these gases, decreases as $I \propto 1/\lambda^4$. Meanwhile, the haze moves toward Rayleigh scattering, which leads to an increase in its backscatter component. Together, this means that the brightness from the lower atmosphere decreases while the brightness at the top of the annulus increases. The increased optical depth of the annuli produces more backscattering than the rest of the haze throughout the atmosphere. The higher altitude also presents a shorter two-way path through the atmosphere, reducing multiple scattering events that could remove the photons from the beam of VIMS. The increase in localized backscatter and the reduction of multiple scattering lead to the annuli being brighter than the surrounding atmosphere.

4.1.3. 700–2000 nm

The backscatter component of weak-particle/aerosol scattering is not particularly intense owing to the lower extinction efficiency of the relatively small scatterers. The extra brightness produced by the annuli is therefore lost in the brightness produced by the highly reflective surface. Not only is the surface brightness ($I/F \approx 10^{-1}$) two to three orders of magnitude greater than the $\Delta I/F$ for the annuli ($\sim 10^{-3}$), but the surface is much more variegated than the atmosphere, making the detection of the small difference between the annuli and the rest of Titan very difficult. Instead, we utilize the methane absorption channels, including ~ 900 and ~ 1150 nm used for our detections. The majority of photons are absorbed at these wavelengths. Those that are not absorbed are scattered by the haze. As before, the increased optical depth at a higher altitude increases backscatter and reduces multiple scattering, producing a localized bright feature.

At longer wavelengths, several complementary effects produce a slow drop-off in differential brightness. Primarily, the intensity of the scattered light drops off as $1 - e^{-\lambda}$ following Beer–Lambert's law. Additionally, the longer-wavelength methane absorption channels are more effective, requiring a lower density of methane to achieve opaqueness. This means that the atmosphere becomes opaque at higher altitudes as wavelength increases. At ~ 2.4 μm the annulus becomes indiscernible from the rest of the atmosphere. The atmosphere becomes essentially opaque at ~ 100 km for 1.2 μm and at ~ 130 km for ~ 2.4 μm, suggesting that the annulus has a minimum altitude of 100–130 km. Altitude constraints for the NPA and EQA are discussed further in the next section. Finally, solar intensity drops off at longer wavelengths, leading to a signal-to-noise ratio so low that it is not possible to discern the annulus in the images or the deviation in the transects.

4.2. Origin and Evolution of the Annuli

4.2.1. Formation of the North Polar Annulus

The NPA occurs at the boundary where the north polar hood was seen until it dissipated during Titan's spring (Le Mouélic et al. 2012). At that time, a bright ring of haze and mist whose opacity smoothly rises from about 51° to 68° north was seen by VIMS bordering the north polar hood (Griffith et al. 2008). While this band is not spectrally or morphologically consistent with our observation of the NPA, it is circumglobal at certain wavelengths and was estimated to be at about 40 km of altitude according to radiative transfer modeling. This band is evidence of the potential for haze to build up at the border of the north polar hood. When the north polar hood began to break up, this band did not immediately dissipate, leaving behind a zone clear of haze and clouds near the pole (Le Mouélic et al. 2012; Rannou et al. 2012).

We propose that the NPA is another manifestation of haze collecting at the mixing boundary encircling the north polar hood. In this scenario, haze is produced in the summer hemisphere and transported to the winter hemisphere. This process forms a polar hood (Rannou et al. 2004; Larson et al. 2015) and gradually builds up an annulus at the boundary of a polar jet or a sharp change in the polar vertical velocities. Titan's polar hoods contain high concentrations of ethane, which is consistent with their location above the arctic circle (Mayo & Samuelson 2005). The polar annuli, however, exist

equatorward of the arctic circle and may not be able to maintain condensed ethane aerosols. As spring comes to the north, the ethane begins to deplete from the polar hoods, entraining accumulated haze with it. Because the polar annuli lack ethane, they persist longer, until they are eventually transported away by the summer meridional circulation.

We also investigated whether the NPA (and the other annuli) could be explained by methane clouds, as nearly global arcs of cloud have been observed with ISS and VIMS (Turtle et al. 2018). We find that there is no obvious correlation between the presence of clouds and the presence of the annuli. In Figure 2(c), we see that the annuli are present while no clouds are visible. We have also seen that the presence, location, and morphology of clouds when seen by VIMS or ISS do not correlate with the presence, location, or morphology of the annuli. We suggest that the annuli and clouds seen in Turtle et al. (2018) may be related by the same (or a similar) mechanism, which acts to corral them into global circular features.

4.2.2. Evolution of the North Polar Annulus

The differential spectrum of the NPA changes as Titan moves further toward northern summer. We see that the entire spectrum gets darker and the bright component shifts redward (Figures 9(B) and 10). We note the similarities between the differential spectra of the NPA over time (Figure 9(B)) and the modeled differential spectra where the haze abundance is increased at several altitudes (Figure 9(C)). As the altitude of the modeled differential spectra increases, the dark component short of 700 nm decreases while shifting spectrally very little. We see the same behavior in the NPA differential spectrum over time. The dark components of the differential spectra of the NPA at $L_S = 40°–50°$, $L_S = 53°–63°$, and $L_S = 78°–88°$ most closely resemble the dark components of the modeled differential spectra at 0–30 km, 20–50 km, and 100–130 km, respectively. We propose that these similarities are indicative of the NPA increasing in altitude as the season progresses. The bright component of the modeled differential spectra also shows some similarities to the observed spectra, but not as much as the dark component. A more complete radiative transfer model is needed to fully quantify how the spectrum of the NPA changes in the way that it does.

This scenario is consistent with the expected change in the meridional circulation (Battalio et al. 2022). As spring turns to summer, the two meridional circulation cells that converge in an upwelling event at the equator transition to a single cell, which rises in the north and subsides in the south (Tokano 2011). We propose that haze originally transported to the north polar hood during the winter and spring months is lofted higher by the summer upwelling at the north. It is possible that the band observed at the boundary of the north polar hood did not simply dissipate, but rather moves to higher altitudes while also changing in abundance, size, fractal dimension, and/or single scattering albedo.

The increase in the semimajor axis of the NPA in Figure 11 may be related to variations in the polar temperature. As the temperature gradient decreases during summer, the weakening strength of the jet and polar vortex could result in larger-amplitude waves dipping farther south (Newman et al. 2011; Lora et al. 2015, 2019) This could also lead to an increase in the ellipticity of the annuli. Determining the ellipticity of the annuli requires additional terms in the sinusoidal function,

which must await constraint by higher-resolution observations than are currently available. Alternatively, as upwelling at the north pole peaks at summer solstice, the increase in velocity may act to move the bounds of NPA farther south. It could also be indicative of the upwelling moving to lower latitudes. This could be a sign of how Titan moves from pole-to-pole circulation at solstice to equator-to-pole circulation at the equinoxes.

4.2.3. Evolution of the Equatorial Annulus

We proposed in Section 4.1 that the dark component of the annuli's differential spectra (shorter than 600 nm) is produced by the haze in the annulus obscuring the bright Rayleigh scattering from the lower atmosphere. If the haze in the annulus is more abundant, it will have a higher optical depth, which will make it more efficient at blocking the illumination from below. Meanwhile, the bright component of the differential spectra (near-IR) of the annuli is produced by the scattering from the top of the annuli. Once again, more haze in the annuli leads to a higher optical depth, which facilitates more backscattering.

We propose that the dark and bright components of the EQA spectra in Figures 9(A) and 10 change intensity in unison from a change of optical depth. The change in optical depth is due to changing haze abundances as a function of season. The EQA is at its brightest and darkest around the vernal equinox. From this we infer that the haze at the equator increases until it reaches a maximum abundance in the annuli around the vernal equinox, and then it begins to decrease. It appears that the EQA becomes least distinguishable from the rest of the atmosphere around the summer and winter solstices. This suggests that the haze abundance in the EQA is similar to the rest of the stratosphere.

4.2.4. Formation of the Equatorial Annulus

If the haze abundance is responsible for the change in intensity of the EQA, then the haze reaches its maximum abundance at the vernal equinox, which coincides with the circulation pattern of upwelling at the equator from the equator-to-pole meridional circulation cell circulation. We suggest that the haze becomes suspended at the convergence of the north and south cells. As the circulation transitions from equator-to-pole to pole-to-pole, the haze that had been accumulating and suspended begins to disperse. What is curious, however, is that we do not see the EQA go away; rather, it persists all the way up to and including at summer solstice. This might suggest that some part of the haze that had been built up during fall remained at the equator. Perhaps this is because of some area of quiescence brought about by gravity or pressure waves, or maybe the circulation in the middle stratosphere is just not effective. In this case horizontal circulation may happen in the troposphere and near the stratopause, flowing in opposite directions, while the center of the stratosphere remains unmixed and undisturbed.

4.3. Using the Annuli to Track the Stratosphere

Given their altitude ($> \sim 130$ km), the annuli are tracers of Titan's zonal stratospheric superrotation and seasonal meridional circulations, as well as the orientation of the stratosphere with respect to the solid body. The annuli can be observed from Earth-based observatories, allowing us to extend the understanding of the stratosphere and meridional circulation a full Titan year. The distribution of secondary annuli

bears a resemblance to zonal wind patterns produced by barotropic waves in Titan's stratosphere based on shallow water modeling (Luz & Hourdin 2003). The secondary annuli may offer accessible observables of Titan's barotropic waves.

4.3.1. The Tilt of Titan's Stratosphere

The tilt of Titan's atmosphere, relative to the tilt of the solid surface, is one of the remaining questions left open after the end of the Cassini mission (Nixon et al. 2018). The mechanism of the tilt and superrotation of Titan's stratosphere are not well understood. Tokano (2010) proposes that the tilt is the result of thermal tides and is only possible if atmospheric waves perturb the circulation. From Figure 13 we see that the observed temporal variation in the azimuthal offset of the normal vector of the annulus from the subsolar vector does not follow the path predicted by Tokano (2010). The most likely explanation is that the weak zonal wind in his GCM affects all three components of AAM in such a way that the azimuth of the tilt turns out to be wrong most of the time. Another possible explanation is that the tilt is not directly responding to thermal tides, unlike the assertion by Tokano (2010). Tokano (2010) discarded the possibility of mixed Rossby-gravity waves as a cause of westward migration of the tilt because the superrotating winds in the upper stratosphere should turn the phase speed of such waves relative to the surface to eastward. However, it is worth mentioning that Battalio & Lora (2021b) predicted the presence of mixed Rossby-gravity waves and equatorial Rossby waves in their GCM. Therefore, the likelihood that Rossby waves affect the precession of the tilt of the annuli cannot be fully dismissed. Achterberg et al. (2008) propose that the tilt facilitates the vertical transport of angular momentum to balance the heat flow and insolation at low latitudes by feedback between the circulation and the heating.

The azimuthal position of the stratosphere shows some correlation with the subsolar longitude. We suggest that the orientation and position of the stratosphere are strongly correlated with the seasons when examined in an inertial reference frame (Figures 12 and 14). There is some indication that the stratosphere reorientates itself throughout the year around a centroid offset by a few degrees from the north polar axis. Assuming that this is correct, we suggest that the centroid about which the stratosphere reorientates itself is itself rotating around the north polar axis. In this scenario the centroid is a seasonal feature (Figure 12, top), while the stratosphere around the centroid may be an orbital or diurnal feature with a much shorter period (Figure 12, bottom). We suggest that our data set supports the proposed mechanism for the tilt suggested in Achterberg et al. (2008).

In Figure 12 we see how the azimuthal position of the stratospheric tilt (the angle in the X-Y plane) is oriented with respect to the north polar axis in an inertial (star-fixed) reference frame. The tilt follows a sinusoid, with a maximum deflection of about $2°$ clockwise at $L_s \approx 25°$. We propose that this sinusoid indicates that the orientation of the stratosphere is dependent on the season rather than on the solar position. We propose that the stratosphere rotates around the north polar axis in response to the subsolar latitude and true anomaly. These results support and expand on the interpretation of Achterberg et al. (2011), which suggested that the stratosphere is fixed in an inertial reference frame. These results imply that the mechanism for the tilt proposed in Achterberg et al. (2008) is seasonally dependent and reorientation at different azimuthal

angles facilitates this process or is a product of the process. Additionally in Figure 14, the points seem to cluster around R. A. $= -2°$ and decl. $= 2°$, suggesting that the stratosphere rotates around an axis offset from the north polar axis. The three peaks in the bottom panel of Figure 12 between -15 and $60°$ relative to the vernal equinox might indicate that this axis is orbiting around the north polar axis and is presenting itself in our data as a second-order waveform.

4.3.2. Testing Rotation Rates

The large difference in the rotation rate of the EQA and the NPA ($0.14 \pm .4$ versus $3.35 \pm .54$) would suggest that the equatorial and polar stratospheres rotate independently of one another. GCMs show that the different latitudes experience different zonal wind velocities in the stratosphere (Newman et al. 2011; Lebonnois et al. 2012; Lora et al. 2015). The simulations show, however, that the peak wind speed is in the winter hemisphere, with the slowest speed experienced in the summer hemisphere. We suspect that the EQA and NPA precession rates are not decoupled. In the top panel of Figure 13 we can see that from $-60°$ to $10°$ relative to vernal equinox the EQA does not precess. Then, from $10°$ to $40°$ after the vernal equinox, the precession rate of the EQA accelerates. If the EQA precession rate were to remain on its course after $L_S = 40°$, we might expect it to look exactly like the precession rate of the NPA. We therefore suggest that the EQA and NPA precess together at the same rate. Furthermore, we suggest that the EQA and NPA are nearly parallel with each other and move in lock step. A more detailed investigation of nearly contemporaneous observations of the EQA and NPA will be needed to verify this hypothesis.

5. Conclusion

The NPA, the EQA, and the SPA are stratospheric seasonal features that provide insight into Titan's circulation mechanisms and patterns. The annuli are unique among Titan features in their refined morphology (as compared to the polar hoods and the north–south asymmetry), their predictability (as compared to clouds), and their scale, which allows for Earth-based observations. From the differential spectra of the annuli, we conclude that the annuli are areas of increased haze. Using spectraltimetric techniques, we determined the minimum altitude of the annuli to be between 100 and 130 km. Triangulation of the NPA is consistent with the spectraltimetry with a modeled median altitude of $H = 217 \pm 2$ km. We tracked the EQA and the NPA over the course of the Cassini mission and investigated their changes in position and spectra.

The annuli are easily observable features that can be used to track the evolution of Titan's stratosphere on seasonal and yearly timescales. The annuli have already been observed with Keck (Roe et al. 2002), and with an expected spatial resolution of 200 km and a spectral range of 600–2300 nm, the annuli should be readily observable with JWST (Nixon et al. 2016). The timing and position of the annuli are controlled by Titan's circulation and dynamic and chemical mixing boundaries. An understanding of the annuli, including how they form and what they are made of, provides insight into the driving forces that control Titan's stratosphere.

The EQA is visible for the entirety of the Cassini mission. The spectra of the EQA increase in absolute contrast to a maximum of about $10°$ of L_S after the vernal equinox. We

suggest that this is evidence of the haze increasing in abundance in the EQA as Titan approaches the vernal equinox. We propose that the EQA is formed by upwelling at the equator where the north and south equator-to-pole meridional circulation cells converge around the vernal equinox. When the meridional circulation cells transition to a single pole-to-pole cell, most of the haze accumulated at the equator is transported poleward. Given the continuous observation of the EQA, we propose that some haze must remain in the middle stratosphere, where wind speeds are possibly low and meridional circulation is stagnant. This is supported by the meridional stream functions shown in Figure 7 of Lebonnois et al. (2012). We see that at $L_S = 123°.8$ (the nearest time to summer solstice) the meridional circulation crosses the equator at ∼300 km. Meanwhile, in the lower stratosphere near 100 km, the meridional circulation is limited to a small cell spanning 20° south and 20° north. In this area we might expect that this small cell continuously circulates any haze that had been lofted during the convergence events seen at $L_S = 8°.9$ and $179°.3$.

We did not observe the SPA despite many opportunities where the viewing geometry would have allowed detection. Because it was detected in 1999–2001, but not during the Cassini mission, we propose that the SPA is a seasonal feature. Thus, if we assume that the polar stratospheres and the circulation are mostly symmetric between the hemispheres, then we can also assume that the NPA is a seasonal feature.

The NPA becomes detectable about 35° of L_S after the vernal equinox and remains present up to the end of the Cassini mission. The spectrum of the NPA is nominally identical to the EQA, but it changes in ways the EQA does not. The darkening of the spectra of the NPA is consistent with our models that suggest that the altitude of the NPA is increasing throughout our observations. The NPA shares its morphology and location with several other north polar features, including the north polar hood. The timing/sequence of the other polar features and the NPA leads us to suggest that the NPA is haze, which was on the border of the north polar hood. As the north pole enters summer, the ethane in the north polar hood falls out, carrying the haze along with it, leaving the NPA as remnant haze occupying the stratosphere on the arctic circle.

An important result of this work is the tracking of the tilt and azimuthal offset of the annuli, and by extension the stratosphere. We found that the tilt of the stratosphere is in the range predicted by Tokano (2010) but does not follow any distinct pattern. We found that the azimuthal position of the stratosphere does not match the prediction from Tokano (2010). The azimuthal position of the stratosphere shows some correlation with the subsolar longitude. We suggest that the orientation and position of the stratosphere are strongly correlated with the seasons when examined in an inertial reference frame (Figures 12 and 14). There is some indication that the stratosphere reorientates itself throughout the year around a centroid offset by a few degrees from the north polar axis. Assuming that this is correct, we suggest that the centroid about which the stratosphere reorientates itself is itself rotating around the north polar axis. In this scenario the centroid is a seasonal feature (Figure 12, top), while the stratosphere around the centroid may be an orbital or diurnal feature with a much shorter period (Figure 12, bottom). We suggest that our data set supports the proposed mechanism for the tilt suggested in Achterberg et al. (2008).

In order to analyze the annuli, we developed (1) a mosaicking routine with aspects of subpixel superresolution, (2) a technique for correcting the striping in the VIMS-Vis data set, and (3) an empirical technique for improving the contrast in a Titan observation. Any data used in this work or any of the above-described techniques can be made available by contacting the first author.

Appendix A
VIMS-Vis Destriping

To remove the striping, we reconstruct what the offsets introduced by the readout electronics would have been. We first sample each line of data that runs perpendicular to the striping on the sample (Figure A1). We apply a smoothing spline based on the LOESS (Appendix B) method to each line. We use a second-degree polynomial to model the local regression and a span of 2/3. The span is the fraction of the total number of data points used for calculating the smoothed value. We subtract the smoothed spline from the data and approximate the spikiness of the data from the stripes in the lines (Figure A2). Stitching the lines back together, with each of their respective smoothed curves removed, produces an approximation of the stripes Figure A3). We know that the offset applied is constant for each sample. We approximate this constant value by taking the median of data along the line dimension (Figure A4). This gives us a single line of data, which we then expand to the original image size, producing a mask for the initial offset (Figure A5). To destripe the data, we subtract Figure A5 from A1 to produce a VIMS image with greatly improved clarity.
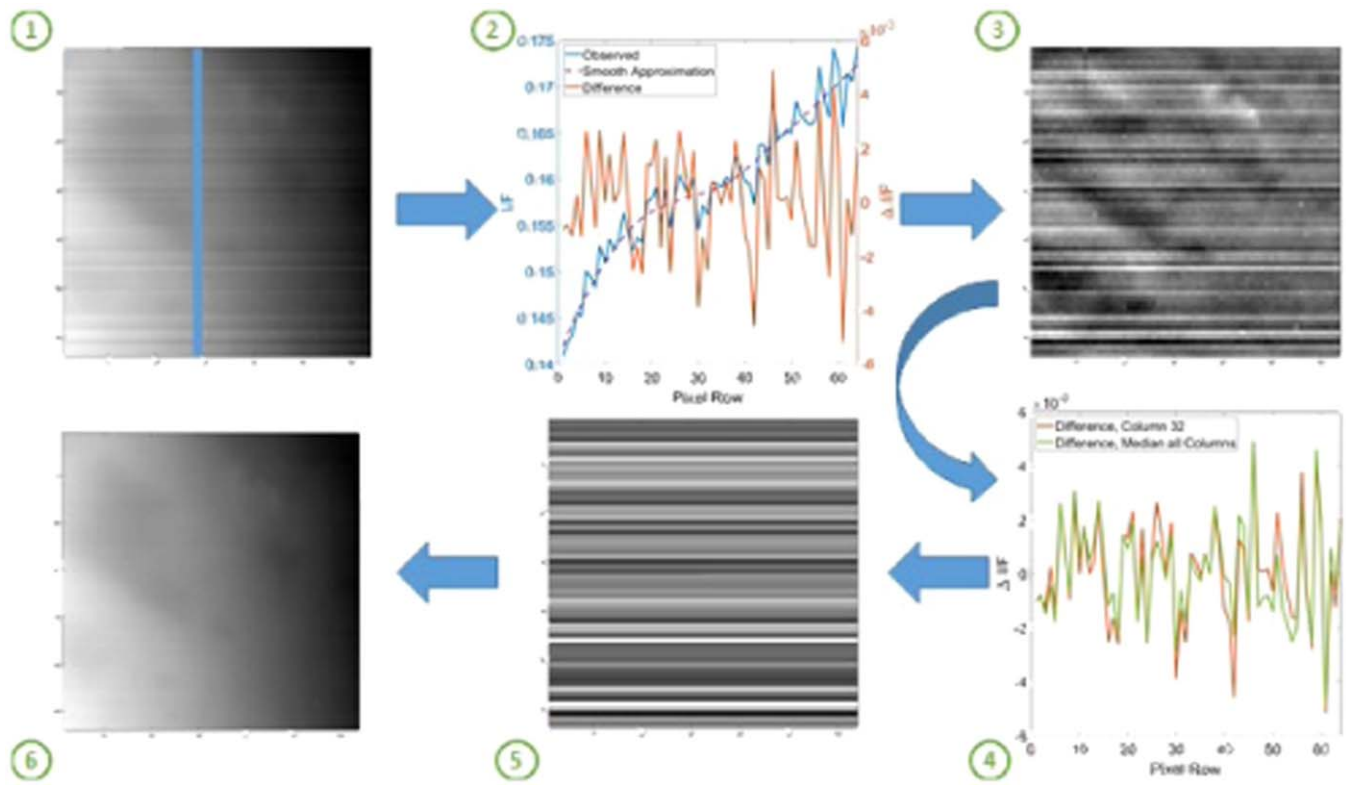
Figure A. Schematic showing the VIMS destriping routine described in Appendix A.

Appendix B
Manifold Correction

The goal of the manifold technique is to remove global scale brightness trends from our observations. We want to remove effects due to illumination geometry and scattering from the haze while preserving compositional and physical properties like grain size and roughness. The predicted brightness due to these effects resembles a curvy surface, which we call a "manifold." To remove effects like viewing geometry and scattering from the VIMS data, we subtract the manifold from the observations. This technique is analogous to flat-field corrections, which are ubiquitous throughout astronomy.

First, we produce subpixel-style superresolution mosaics and project them into an orthographic view. We have to produce a manifold for each channel in VIMS because the amount and type of scattering in the atmosphere vary with wavelength. For each channel we randomly sample 100 pixels from the mosaic. We fit a locally estimated scatterplot smoothing function (LOESS) to the data points, where the independent variables are the row and column location of the pixel in the mosaic, and the dependent variable is the pixel brightness. The LOESS method fits a low-degree polynomial to a subset of the data at each point in the range of the data set. The polynomial is fitted using weighted least squares, giving more weight to points near the point whose response is being estimated and less weight to points farther away (Savitzky & Golay 1964; Cleveland 1979). We then repeat this process 100 times, each time selecting 100 random pixels from the mosaic, for each channel. This produces 100 manifolds, which we take the average of to produce the final manifold.

By sampling only 100 pixels from our mosaic (which are at least 400,000 pixels in total), we nullify all small-scale variations in data, like those caused by surface composition. The randomly sampled pixels will be separated by about 730 km on average, which is twice as wide as Menrva crater, one of the largest features on Titan's surface. Doing this 100 times through bootstrapping provides a good estimate of the underlying parameters for the brightness trend on Titan. This technique is flexible in many ways, including in the number of data points sampled, how many Monte Carlo runs are made, the wavelengths corrected, and the polynomial degree and weighting of the LOESS function.

Appendix C
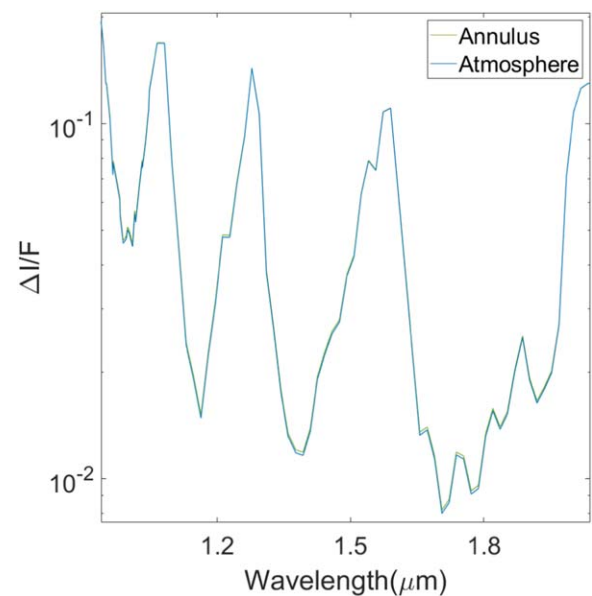
Figure C. Zoom-in of the modeled atmospheric spectra and the modeled annulus spectra from Figure 3. The difference between the two spectra is less than the line width at certain wavelengths.

Appendix D

Table 1
Details of Every Detection of the Annuli

Flyby	Rev	CA UTC	CA Altitude (km)	CA Ephemeris Time	Planetocentric Longitude of the Sun (L_S)	Average Incidence (deg)	Average Emission (deg)	Average Phase (deg)	Central Longitude (deg)	Average Latitude (deg)	Average Pixel Scale (km^2)	Tilt from North Pole (deg)	Prime Meridian Offset (deg, E+)	Subsolar Longitude Offset (deg, E+)	# of Longitude Bins
								North Polar							
T079	TI158	2011-12-13T20:11:23	3 583.241 3	377 079 149.2	28.41	54.69	68.8	19.26	160.27	66.96	77.37				1
T087	TI174	2012-11-13T10:22:08	973.650 52	406074195	39.17	86.21	49.6	131.11	−54.23	65.28	82.11				4
T088	TI175	2012-11-29T08:56:59	1 014.693 4	407 451 486.1	39.66	82.54	43.81	126.19	−68.06	68.85	109.08				2
T089	TI181	2013-02-17T01:56:35	1 978.042 3	414338262	42.19	84.54	35.21	117	−46.05	71.35	157.9	4.76	−148.86	42.8	11
T090	TI185	2013-04-05T21:43:30	1 400.076 1	418 470 277.6	43.7	86.63	37.13	108.86	−36.78	67.95	59.31	2.63	36.93	−133.18	17
T091	TI190	2013-05-23T17:32:55	970.052 55	422 602 441.7	45.21	63.7	45.17	105.01	−113.93	69.63	120.39	1.45	145.81	−26.03	8
T092	TI194	2013-07-10T13:21:47	963.786 73	426 734 573.9	46.7	76.96	29.5	97.53	−73.07	68.79	100.32	1.04	48.07	−125.51	17
T093	TI195	2013-07-26T11:56:22	1 399.697 9	428111849	47.2	81.42	20.11	90.41	−49.04	66.1	61.42	1.64	52.23	−121.96	25
T094	TI197	2013-09-12T07:43:56	1 396.765 3	432243903	48.71	72.86	21.35	83.1	−44.12	67.57	44.02	2.13	38.62	−137.35	28
T095	TI198	2013-10-14T04:56:27	960.758 29	434998654	49.7	63.33	36.86	76.56	95.32	67	86.54	2.67	30.1	−147.04	35
T096	TI199	2013-12-01T00:41:19	1 400.035 4	439 130 545.8	51.19	61.83	23.53	66.13	−77.15	65.5	43.51	3.73	24.2	−154.76	36
T097	TI200	2014-01-01T21:59:41	1 399.810 4	441885648	52.18	62.89	19.95	59.94	−92.06	65.69	78.62	3.61	55.66	−124.39	36
T098	TI201	2014-02-02T19:12:38	1 235.470 6	444640425	53.17	71.86	34.72	51.74	−34.07	66.41	98.89	3.59	48.03	−133.19	36
T099	TI202	2014-03-06T16:26:47	1 499.789 9	447395274	54.16	60.41	29.14	43.04	−66.15	69.17	134.98	3.38	68.39	−113.99	22
T100	TI203	2014-04-07T13:41:14	963.449 34	450150141	55.16	61.96	38.6	34.27	−51.81	68.04	58.05	3.35	42.69	−140.85	28
T101	TI204	2014-05-17T16:12:15	2 991.882 4	453615202	56.4	87.01	29.86	109.5	99.55	66.71	110.8	1.19	−142.66	−142.04	11
T102	TI205	2014-06-18T13:28:25	3 658.690 5	456370172	57.39	84.11	34.45	104.14	70.52	66.15	79.78	0.85	−152.88	−153.39	17
T103	TI206	2014-07-20T10:40:58	5 103.283 1	459 124 925.1	58.38	74.41	37.43	99.95	30.52	66.73	83.72	3.03	−138.85	−140.55	24
T104	TI207	2014-08-21T08:09:09	964.103 3	461880616	59.36	77.77	31.85	103.26	95.2	64.14	44.64	1.65	−127.36	−130.01	17

Table 1
(Continued)

Flyby	Rev	CA UTC	CA Altitude (km)	CA Ephemeris Time	Planetocentric Longitude of the Sun (L_S)	Average Incidence (deg)	Average Emission (deg)	Average Phase (deg)	Central Longitude (deg)	Average Latitude (deg)	Average Pixel Scale (km²)	Tilt from North Pole (deg)	Prime Meridian Offset (deg, E+)	Subsolar Longitude Offset (deg, E+)	# of Longitude Bins
T105	TI208	2014-09-22T05:23:19	1 401.501 6	464635466	60.34	62.97	42.2	110.48	59.9	65.89	39.78	0.28	−42.95	−46.78	18
T106	TI209	2014-10-24T02:40:30	1 013.168 4	467390497	61.32	82	42.51	119.77	112.2	66.38	60.52	1.02	−101.1	−106.05	13
T107	TI210	2014-12-10T22:26:35	980.572 19	471 522 462.4	62.79	94.3	35.54	125.85	153.02	67.83	89.29	0.06	−0.03	−6.83	5
T119	TI235	2016-05-06T16:54:37	969.201 5	515 825 744.7	78.42	83.96	42.9	121.75	104.13	65	54.45	1.58	70.48	103.41	10
T120	TI236	2016-06-07T14:06:17	974.555 42	518 580 444.9	79.39	85.08	34.14	114.78	110.67	64.5	71.57	1.47	78.43	110.11	8
T121	TI238	2016-07-25T09:58:23	975.407 36	522 712 770.8	80.84	82.05	36.62	112.29	97.54	63.17	64.4	0.66	69	98.88	16
T122	TI239	2016-08-10T08:30:53	1 698.358 2	524 089 920.8	81.34	88.69	29.92	111.84	106.87	63.95	143.08	1.13	25.46	54.66	11
T123	TI243	2016-09-27T04:16:59	1 775.659 2	528221887	82.77	67.77	45.93	112	61.43	64.83	69.29	0.62	146.1	173.41	8
T124	TI248	2016-11-13T23:55:56	1 585.323 9	532 353 423.8	84.21	64.59	49.77	112.65	50.88	61.26	107.16	1.15	−40.36	−15.05	5
nT261	TI261	2017-02-17T13:10:26	186 795.47	540 609 095.4	87.09	52.84	36.6	78.03	−66.31	66.57	109.41	1.87	88	107.36	14
nT262	TI262	2017-02-17T19:41:26	220 499.08	540 632 554.7	87.1	62.33	35.93	85.05	−22.58	65.17	133.8	3.3	69.19	94.66	25
nT283	TI283	2017-07-10T13:50:53	264 321.55	552 966 722.3	91.4	48.91	23.94	55.67	−15.45	66.54	155.08	3.63	73	76.7	19
nT288	TI288	2017-08-11T05:04:11	194 993.55	555 699 920.5	92.36	55.89	30.81	71.73	31.21	66.47	118.68	0.57	83.39	80.23	11
nT292	TI292	2017-09-11T19:04:49	119 734.92	558 428 758.2	93.3	69.87	29.57	84.68	−68.04	67.29	72.39	3.53	−103.57	−114.72	14
Flyby	Rev	CA UTC	CA Altitude (km)	CA Ephemeris Time	Planetocentric Longitude of the Sun (L_S)	Average Incidence (Deg)	Average Emission (Deg)	Average Phase (Deg)	Central Longitude (Deg)	Average Latitude (Deg)	Average Pixel Scale (km²)	Tilt from North Pole (Deg)	Prime Meridian Offset (Deg, E+)	Subsolar Longitude Offset (Deg, E+)	# of Longitude Bins
					Equatorial										
T00A	TI00A	2004-10-26T15:30:05	1 174.330 6	152076669	297.26	40.84	26.45	19.97	−127.87	−7.54	70.95	1.53	106.02	−98.09	8
T00B	TI00B	2004-12-13T11:38:15	1 192.669 9	156 209 959.6	299.03	44.16	20.53	56.83	−52.61	−0.53	56.37	0.12	−141.42	−61.56	6
T003	TI003	2005-02-15T06:57:53	1 578.974 6	161 722 737.3	301.4	33.54	24.86	13.25	−137.36	−5.31	46.56	4.19	110.84	−89.49	9
T004	TI005	2005-03-31T20:05:16	2 403.893 6	165 571 580.1	303.06	37.27	25.61	15.82	−140.4	−4.8	28.03	5.63	115.77	−86.38	10

Table 1
(Continued)

Flyby	Rev	CA UTC	CA Altitude (km)	CA Ephemeris Time	Planetocentric Longitude of the Sun (L_S)	Average Incidence (deg)	Average Emission (deg)	Average Phase (deg)	Central Longitude (deg)	Average Latitude (deg)	Average Pixel Scale (km^2)	Tilt from North Pole (deg)	Prime Meridian Offset (deg, E+)	Subsolar Longitude Offset (deg, E+)	# of Longitude Bins
T005	TI006	2005-04-16T19:07:16	1 359.185 5	166950500	303.65	54.11	23.32	57.12	−32.98	−3.1	28.12	0.35	51.89	131.46	8
T006	TI013	2005-08-22T08:53:38	3 660.731 8	177 972 881.9	308.36	48.76	23.57	52.66	−27.62	−0.9	41.36	0.65	−117.04	−42.08	7
T007	TI014	2005-09-07T04:01:28	83 235.56	179 337 751.7	308.95	47.63	24.07	51.93	−31.65	−1.42	74.69	2.34	−135.32	−64.31	8
T008	TI017	2005-10-28T04:15:25	1 352.876 1	183 744 988.8	310.81	32.39	24.59	23.54	−138.2	−5.36	65.17	3.34	120.95	−98.26	11
T009	TI019	2005-12-26T18:59:26	10 411.572	188895630	313.01	25	24.2	27.13	−42.06	−1.93	44.49	2.17	−113.75	−69.27	10
T010	TI020	2006-01-15T11:41:26	2 043.032 2	190 597 350.9	313.73	43.96	24.51	37.79	−151.46	−5.65	24.62	2.61	118.01	−113.56	11
T011	TI021	2006-02-27T08:25:18	1 812.311 4	194 300 783.6	315.29	29.83	25.75	18.17	−14.14	−1.86	112.98	3.79	−101.6	−86.97	13
T012	TI022	2006-03-19T00:05:55	1 949.351	195 998 820.6	316.02	51.77	24.99	65.01	−142.81	−3.17	32.31	6.01	141.32	−121.09	11
T013	TI023	2006-04-30T20:37:28	5 735.424 2	199 701 513.3	317.59	36.53	20.29	39.7	−10.78	−2.56	16.94	0.22	80.93	64.59	6
T014	TI024	2006-05-20T12:18:11	1 879.178 5	201399556	318.3	63.07	33.15	91.51	−119.98	−3.06	105.32				1
T015	TI025	2006-07-02T09:20:47	1 906.160 9	205 104 112.1	319.86	47.05	25.06	61.53	10.59	−4.36	93.78	0.84	−76.12	−122.92	6
T016	TI026	2006-07-22T00:25:26	950.385 67	206799991	320.6	52.87	30.76	59.39	2.03	1.9	79.66	4.1	−89.86	−54.3	7
T017	TI028	2006-09-07T20:16:51	999.713 19	210932276	322.33	46.94	23.72	62.92	7.47	0	47.34	1.66	−100.42	−66.74	5
T018	TI029	2006-09-23T18:58:48	960.198 92	212 309 993.5	322.92	35.17	41.28	64.49	−8.17	−4.97	73.94				4
T019	TI030	2006-10-09T17:30:07	980.047 47	213687072	323.5	46.57	40.81	65.03	5.44	−1.83	81.26	0.92	−98.11	−65.7	5
T020	TI031	2006-10-25T15:58:07	1 029.512 2	215063952	324.07	36.2	45.98	71.81	−4.31	1.87	74.86	1.75	90.75	122.4	5
T021	TI035	2006-12-12T11:41:31	1 000.284 7	219195756	325.81	58.62	34.79	67.41	21.76	1.3	95.85	3.2	−80.38	−50.71	5
T025	TI039	2007-02-22T07:24:34	86 205.694	225 401 139.6	328.38	24.79	55.63	69.36	126.85	−3.17	112.45				2
T026	TI040	2007-03-10T01:49:00	980.607 62	226763405	328.95	30.35	49.26	62	127.31	−5.45	68.68	3.95	50.28	−105.51	7
T027	TI041	2007-03-26T00:23:27	1 010.089 8	228 140 672.1	329.53	24.87	46.2	53.24	135.84	−6.95	115.47	0.7	0.02	−156.42	7
T028	TI042	2007-04-10T22:58:00	991.146 26	229 517 944.8	330.1	28.7	42.45	45.81	128.52	−6.15	74	3.05	45.75	−111.34	10
T029	TI043	2007-04-26T21:32:58	981.179 96	230895243	330.67	30.56	32.86	37.25	129.21	−4.42	89.58	4.43	34.81	−122.91	8

Table 1
(Continued)

Flyby	Rev	CA UTC	CA Altitude (km)	CA Ephemeris Time	Planetocentric Longitude of the Sun (L_S)	Average Incidence (deg)	Average Emission (deg)	Average Phase (deg)	Central Longitude (deg)	Average Latitude (deg)	Average Pixel Scale (km^2)	Tilt from North Pole (deg)	Prime Meridian Offset (deg, E+)	Subsolar Longitude Offset (deg, E+)	# of Longitude Bins
T030	TI044	2007-05-12T20:09:58	959.584 86	232272663	331.25	31.07	27.95	29.29	133.41	−2.6	82.7	6.44	54.11	−104.23	12
T031	TI045	2007-05-28T18:51:55	2 299.088 5	233 650 380.2	331.81	35.39	32.69	27.47	127.37	−4.86	29.45	3.4	50.88	−107.98	11
T032	TI046	2007-06-13T17:46:11	965.396 65	235028836	332.39	32.08	25.94	16.15	131.63	−3.3	58.83	1.56	68.97	−90.22	9
T033	TI047	2007-06-29T16:59:46	1 932.782 6	236408451	332.95	26.72	19.52	13.69	137.71	−3.14	23.28	4.17	60.02	−99.2	11
T034	TI048	2007-07-19T01:11:20	1 331.914 5	238 079 545.2	333.65	38.73	23.51	58.26	43.25	−1.15	25.18				3
T035	TI049	2007-08-31T06:32:36	3 324.615 5	241 814 020.8	335.19	26.82	17.15	26.87	159.3	−1.97	26.5	2.64	74.92	−113.88	10
T036	TI050	2007-10-02T04:42:43	973.489 1	244 572 228.1	336.33	35.94	26.9	32.54	134.06	−3.48	91.04	3.53	65.33	−123.77	10
T037	TI052	2007-11-19T00:47:25	999.652 91	248705310	338.03	36.22	16.89	40.66	142.73	−2.75	49.56	4.55	65.53	−125.14	8
T038	TI053	2007-12-05T00:06:50	1 298.834 1	250 085 274.9	338.59	31.41	19.37	44.55	158.82	−3.48	17.42	1.9	73.28	−117.31	9
T039	TI054	2007-12-20T22:57:55	969.950 23	251463540	339.17	46.04	32.55	50.13	134.06	−5.92	93.88	0.07	120.53	−70.43	8
T040	TI055	2008-01-05T21:30:19	1 014.118 2	252 840 684.6	339.72	38.06	21.11	55.98	156.25	−6.22	14.92	5.77	59.6	−132.02	9
T041	TI059	2008-02-22T17:32:07	999.872 23	256 973 591.9	341.42	46.94	35.5	66.19	139.27	−6.33	82.74	5.16	59.89	−133.31	7
T042	TI062	2008-03-25T14:27:48	999.447 82	259727333	342.54	53.8	23.75	72.98	141.59	−6.17	24.96	0.69	−132.47	32.88	7
T044	TI069	2008-05-28T08:24:32	1 399.989 7	265 235 137.1	344.79	44.41	51.07	89.45	146.68	0.1	105.68				3
T046	TI091	2008-11-03T17:35:23	1 105.099 8	279 005 787.9	350.33	51.51	44.65	81.13	−98.42	0.17	90.41	3.03	165.25	−38.85	6
T047	TI093	2008-11-19T15:56:28	1 023.290 7	280 382 252.9	350.89	49.5	45.2	84.76	−101.92	−7.91	57.73				3
T048	TI095	2008-12-05T14:25:45	960.510 53	281759210	351.44	46.96	47.03	77.68	−101.48	−5.38	85.57				3
T049	TI097	2008-12-21T12:59:52	970.886 78	283136457	351.99	42.61	45.63	71.26	−104.01	−1.53	89.57	3.9	154.79	−51.43	6
T050	TI102	2009-02-07T08:50:52	967.024 19	287 268 717.8	353.64	42.42	49.62	70.66	−101.92	−0.9	118.46	0.88	0	152.1	5
T051	TI106	2009-03-27T04:43:36	962.880 46	291 401 082.3	355.29	44.2	53.04	75.21	−98.58	−5.04	127.55				3
T053	TI109	2009-04-20T00:20:45	3 598.575 5	293 458 911.1	356.14	37.63	56.47	68.02	62.41	−3.46	110.16				3
T054	TI110	2009-05-05T22:54:15	3 242.262 8	294 836 120.9	356.68	24.4	55.23	62.78	47.87	0.88	106.01	4.72	−40.04	−73.18	7

Table 1
(Continued)

Flyby	Rev	CA UTC	CA Altitude (km)	CA Ephemeris Time	Planetocentric Longitude of the Sun (L_S)	Average Incidence (deg)	Average Emission (deg)	Average Phase (deg)	Central Longitude (deg)	Average Latitude (deg)	Average Pixel Scale (km^2)	Tilt from North Pole (deg)	Prime Meridian Offset (deg, E+)	Subsolar Longitude Offset (deg, E+)	# of Longitude Bins
T055	TI111	2009-05-21T21:26:41	965.623 78	296 213 267.1	357.24	23.79	49.97	52.13	29.55	−1.55	194.95	1.44	−60.71	−94.47	7
T056	TI112	2009-06-06T20:00:00	967.717 2	297 590 466.1	357.79	33.54	48.82	44.21	49.64	−2.47	163.46	3.56	−57.21	−91.59	10
T057	TI113	2009-06-22T18:32:35	955.214 66	298967621	358.32	29.42	44.67	36.87	35.92	−1.9	91.92	3.41	−53.53	−88.53	10
T058	TI114	2009-07-08T17:04:03	966.055 3	300 344 709.3	358.86	27.86	38.62	29.9	51.37	−1.94	49.59	4.16	−60.44	−96.09	11
T059	TI115	2009-07-24T15:34:03	956.582 69	301 721 709.1	359.41	18.39	27.89	22.52	30.89	−4.11	36.5	3.98	−65.48	−101.8	6
T061	TI117	2009-08-25T12:51:37	960.837 48	304 476 763.6	0.5	26.14	32.34	12.95	30.41	−3.18	22.72	2.76	−62.07	−99.44	13
T062	TI119	2009-10-12T08:36:24	1 299.964 9	308 608 650.2	2.14	31.55	30.4	10.5	10.19	−3.17	129.31	3.12	−67.91	−107.04	11
T063	TI122	2009-12-12T01:03:14	4 847.710 8	313 851 859.8	4.19	42.19	23.3	46.81	145.57	−1.91	55.65	1.98	40.56	−70.32	9
T064	TI123	2009-12-28T00:16:58	951.817 66	315 231 484.6	4.73	40.78	22.31	44.29	147.41	−2.15	30.55	3.33	34.49	−76.37	8
T065	TI124	2010-01-12T23:10:36	1 074.516	316 609 901.9	5.27	27.33	38.94	44.17	113.07	−2.02	56.58	4.93	40.89	−70.26	9
T066	TI125	2010-01-28T22:28:50	7 486.939 1	317 989 795.7	5.81	38.7	25.2	43.37	140.44	−0.31	75.38	0.89	0	−111.05	9
T067	TI129	2010-04-05T15:50:54	7 437.318 4	323 754 719.8	8.06	21.12	21.04	13.61	36.75	−3.68	51.67	2.1	−65.1	−111.75	12
T068	TI131	2010-05-20T03:24:20	1 398.006 7	327 597 926.3	9.56	31.66	25.9	31.55	133.37	−2.03	118.34	2.52	46.14	−77.6	10
T069	TI132	2010-06-05T02:26:27	2 042.953	328976853	10.09	31.33	35.09	31.05	117.8	−1.26	71.79	3.84	50.77	−73.12	11
T070	TI133	2010-06-21T01:27:43	878.567 51	330 355 728.9	10.62	33.88	25.04	32.24	146.06	−2	36.56	3.05	48.82	−75.25	11
T071	TI134	2010-07-07T00:22:45	1 004.078 5	331 734 231.1	11.16	36.43	23.32	35.03	143.59	−2.41	76.2	2.08	51.21	−73.12	9
nT136	TI136	2010-08-11T13:35:03	417 252.75	334 805 769.2	12.35	48.94	23.86	56.38	78.24	−1.47	178.1	2.1	0.01	−42.77	6
T072	TI138	2010-09-24T18:38:41	8 177.99	338 625 587.1	13.81	27.09	30.66	24.09	114.76	−3.06	17.12	0.54	0.01	−125.96	9
T074	TI145	2011-02-18T16:04:11	3 651.096 8	351 317 117.2	18.69	33.33	29.51	31.36	16.38	−4.23	150.65	1.71	−70.15	−124.13	11
T075	TI147	2011-04-19T05:00:39	10 052.942	356461305	20.64	31.88	32.02	18.21	127.75	−2.7	77.18	1.54	58.84	−92.75	11
T076	TI148	2011-05-08T22:53:44	1 872.807 1	358 167 290.5	21.28	31.33	22.26	42.38	36.87	−4.94	24.59	3.48	−60.78	−127.14	9
T077	TI149	2011-06-20T18:32:00	1 358.992 4	361 866 786.6	22.68	33.57	31.88	21.17	126.38	−3.95	51.2	2.13	76.03	−104.96	10

Table 1
(Continued)

Flyby	Rev	CA UTC	CA Altitude (km)	CA Ephemeris Time	Planetocentric Longitude of the Sun (L_S)	Average Incidence (deg)	Average Emission (deg)	Average Phase (deg)	Central Longitude (deg)	Average Latitude (deg)	Average Pixel Scale (km^2)	Tilt from North Pole (deg)	Prime Meridian Offset (deg, E+)	Subsolar Longitude Offset (deg, E+)	# of Longitude Bins
T078	TI153	2011-09-12T02:50:06	5 821.661 5	369 067 871.9	25.4	52.85	30.6	75.85	46.71	−5.86	57.86	4.22	−34.8	−136.56	6
T079	TI158	2011-12-13T20:11:23	3 583.241 3	377 079 149.2	28.41	33.33	22.99	23.23	144.81	−4.65	16.84	3.15	69.1	−102.1	12
T081	TI160	2012-01-30T13:39:48	31 130.577	381 202 854.1	29.96	34.31	38.73	28.17	−140.56	−3.89	73.62	3.36	74.4	−100.7	12
T082	TI161	2012-02-19T08:43:17	3 803.185	382 913 062.9	30.59	53.04	21.81	63.85	35.22	−4	38.83	3.63	−35.13	−123.89	6
T083	TI166	2012-05-22T01:10:11	953.990 5	390 921 076.9	33.58	32.06	27.24	21.93	134.49	−4.56	71.74	1.92	50.92	−108.15	11
T084	TI167	2012-06-07T00:07:21	959.347 58	392 299 706.8	34.09	37.44	37.38	28.4	119.55	−4.26	103.69	4.02	60.22	−99.09	11
T085	TI169	2012-07-24T20:03:07	1 012.449 8	396 432 253.9	35.61	26.95	20.75	33.04	155.36	−3.89	15.92	1.45	71.49	−89.43	11
T086	TI172	2012-09-26T14:35:38	956.550 55	401942205	37.66	34.94	32.96	47.11	136.86	−3.54	128.58	0.64	49.84	−113.24	8
T087	TI174	2012-11-13T10:22:08	973.650 52	406074195	39.17	31.65	38.91	52.92	146.05	−4.43	75.31	2.43	53.44	−111.4	10
T088	TI175	2012-11-29T08:56:59	1 014.693 4	407 451 486.1	39.66	29.98	28.63	58.32	157.04	−3.17	19.94	1.95	55.57	−109.87	6
T089	TI181	2013-02-17T01:56:35	1 978.042 3	414338262	42.19	40.74	38.25	68.48	113.47	−5.54	181.36				2
T090	TI185	2013-04-05T21:43:30	1 400.076 1	418 470 277.6	43.7	41.84	40.49	73.85	136.55	−7.03	49.82	0.06	0	−170.11	5
T091	TI190	2013-05-23T17:32:55	970.052 55	422 602 441.7	45.21	35.4	46.7	80.58	140.05	−6.98	94.14				1
T101	TI204	2014-05-17T16:12:15	2 991.882 4	453615202	56.4	40.69	38.55	67.89	−15.37	−6.79	130.88				3
T102	TI205	2014-06-18T13:28:25	3 658.690 5	456370172	57.39	36.77	44.8	75.21	−15.73	−7.18	120.87				2
T106	TI209	2014-10-24T02:40:30	1 013.168 4	467390497	61.32	33.76	35.88	66.44	−4.72	−5.55	50.22				3
T107	TI210	2014-12-10T22:26:35	980.572 19	471 522 462.4	62.79	40.16	31.86	59.21	−7.63	−1.5	90.91	7.58	80.23	73.43	5
T108	TI211	2015-01-11T19:48:35	970.385 16	474277782	63.77	39.07	27.95	52.07	−10.92	−4.77	31.13	2.13	−100.52	−108.37	5
T109	TI212	2015-02-12T17:08:04	1 200.149 1	477 032 951.1	64.75	24.41	22.94	42.12	−1.28	6.67	13.6				4
T112	TI218	2015-07-07T08:09:50	10 952.196	489 528 658.1	69.17	37.48	19.64	24.85	−26.09	−4.98	42.5				3
T114	TI225	2015-11-13T05:46:31	11 927.57	500 665 658.9	73.1	35.63	19.64	28.11	−25.85	−7.69	39.82				3
T116	TI231	2016-02-01T01:00:05	1 398.535 8	507 560 472.7	75.52	32.56	11.54	32.21	−25.06	−5.26	36.88				2

Table 1
(Continued)

Flyby	Rev	CA UTC	CA Altitude (km)	CA Ephemeris Time	Planetocentric Longitude of the Sun (L_S)	Average Incidence (deg)	Average Emission (deg)	Average Phase (deg)	Central Longitude (deg)	Average Latitude (deg)	Average Pixel Scale (km²)	Tilt from North Pole (deg)	Prime Meridian Offset (deg, E+)	Subsolar Longitude Offset (deg, E+)	# of Longitude Bins
								Secondary 1							
T062	TI119	2009-10-12T08:36:24	1 299.964 9	308 608 650.2	2.14	55.31	56.25	10.69	9.58	57.77	177.46	3.85	19.01	−20.12	10
T067	TI129	2010-04-05T15:50:54	7 437.318 4	323 754 719.8	8.06	49.14	50.53	14.42	21.25	47.94	79.58				3
T071	TI134	2010-07-07T00:22:45	1 004.078 5	331 734 231.1	11.16	49.9	39.91	34.91	159	32.32	84.03				3
T076	TI148	2011-05-08T22:53:44	1 872.807 1	358 167 290.5	21.28	46.32	51.75	46.18	34.07	47.25	64.11				3
T079	TI158	2011-12-13T20:11:23	3 583.241 3	377 079 149.2	28.41	43.06	52.61	18.97	142.38	52.31	55.65	1.56	60.19	−111.01	7
T082	TI161	2012-02-19T08:43:17	3 803.185	382 913 062.9	30.59	54.82	47.6	62.79	31.77	43.86	62.07				4
T098	TI201	2014-02-02T19:12:38	1 235.470 6	444640425	53.17	35.97	18.94	52.16	−148.08	51.55	94.63				4
T100	TI203	2014-04-07T13:41:14	963.449 34	450150141	55.16	33.88	14.63	34.86	−153.57	49.28	54.18	2.42	118.8	−64.74	6
T114	TI225	2015-11-13T05:46:31	11 927.57	500 665 658.9	73.1	29.19	51.91	27.2	−3.79	39.47	87.69				3
nT264	TI264	2017-03-05T11:44:03	489 890.93	541 986 902.8	87.57	29.73	18.25	42.71	−28.68	51.78	197.65	2.5	−114.84	−95.99	6
TI126	TI270	2017-04-22T05:52:13	980.236 27	546 113 356.1	89.01	61.52	52.98	111.94	52.75	47.52	99.6				4

Flyby	Rev	CA UTC	CA Altitude (km)	CA Ephemeris Time	Planetocentric Longitude of the Sun (L_S)	Average Incidence (Deg)	Average Emission (Deg)	Average Phase (Deg)	Central Longitude (Deg)	Average Latitude (Deg)	Average Pixel Scale (km²)	Tilt from North Pole (Deg)	Prime Meridian Offset (Deg, E+)	Subsolar Longitude Offset (Deg, E+)	# of Longitude Bins
								Secondary 2							
T00A	TI00A	2004-10-26T15:30:05	1 174.330 6	152076669	297.26	43.1	23.85	19.58	−159.81	18.68	89.13				1
T008	TI017	2005-10-28T04:15:25	1 352.876 1	183 744 988.8	310.81	42.52	21.73	23.16	−163.23	9.42	62.06				3
T036	TI050	2007-10-02T04:42:43	973.489 1	244 572 228.1	336.33	53.8	26.32	32.28	136.42	18.44	89.87				4
T037	TI052	2007-11-19T00:47:25	999.652 91	248705310	338.03	48.99	16.04	39.58	145.28	17.64	36.84				2
T071	TI134	2010-07-07T00:22:45	1 004.078 5	331 734 231.1	11.16	49.9	39.91	34.91	159	32.32	84.03				3
T083	TI166	2012-05-22T01:10:11	953.990 5	390 921 076.9	33.58	23.06	27.05	22.14	130.19	11.54	70.46				1

Table 1

(Continued)

Flyby	Rev	CA UTC	CA Altitude (km)	CA Ephemeris Time	Planetocentric Longitude of the Sun (L_S)	Average Incidence (deg)	Average Emission (deg)	Average Phase (deg)	Central Longitude (deg)	Average Latitude (deg)	Average Pixel Scale (km²)	Tilt from North Pole (deg)	Prime Meridian Offset (deg, E+)	Subsolar Longitude Offset (deg, E+)	# of Longitude Bins
T098	TI201	2014-02-02T19:12:38	1 235.470 6	444640425	53.17	40.17	47.3	52.26	−127.24	15.44	120.7	0.55	−0.04	178.74	6
T099	TI202	2014-03-06T16:26:47	1 499.789 9	447395274	54.16	28.64	38.65	43.33	−133.43	19.24	169.07	0.17	−0.01	177.61	7
T100	TI203	2014-04-07T13:41:14	963.449 34	450150141	55.16	27.94	37.78	35.19	−135.75	15.4	61.86	0.04	0	176.46	10
T107	TI210	2014-12-10T22:26:35	980.572 19	471 522 462.4	62.79	20.67	51.04	59.5	−5.6	18.36	109.36				2
T108	TI211	2015-01-11T19:48:35	970.385 16	474277782	63.77	27.07	45.83	52.46	−10.82	20.07	33.53	1.65	−104.06	−111.91	9
T109	TI212	2015-02-12T17:08:04	1 200.149 1	477 032 951.1	64.75	45.53	29.88	41.8	−32.66	8.94	17.44				4
T110	TI213	2015-03-16T12:59:36	2 274.981 7	479 788 255.4	65.72	33.43	19.31	36.4	−18.59	17.67	13.92	4.38	−119.6	−129.61	5
T111	TI215	2015-05-07T20:38:58	2 722.237 4	484 311 090.4	67.33	49.1	23.16	65.69	−134.97	17.69	22.26	2.79	135.65	−134.3	8
T112	TI218	2015-07-07T08:09:50	10 952.196	489 528 658.1	69.17	25.45	24.21	25.75	−15.88	19.14	58.49	2.19	−104.01	−92.53	6
T114	TI225	2015-11-13T05:46:31	11 927.57	500 665 658.9	73.1	28.62	17.41	29.66	−38.52	−1.47	34.56				3
T116	TI231	2016-02-01T01:00:05	1 398.535 8	507 560 472.7	75.52	19.62	27.91	32.81	−23.67	14.43	37.39	6.03	−109.79	−73.44	5
T119	TI235	2016-05-06T16:54:37	969.201 5	515 825 744.7	78.42	27.94	35.09	53.8	−0.16	8.45	119				1
T124	TI248	2016-11-13T23:55:56	1 585.323 9	532 353 423.8	84.21	41.82	40.87	69.7	−55.84	2.88	44.31				4
T125	TI250	2016-11-29T19:16:29	3 159.020 5	533729740	84.69	47.79	37.41	68.32	−66.49	10.38	32.4	1.33	−150.44	−126.03	5
TI126	TI270	2017-04-22T05:52:13	980.236 27	546 113 356.1	89.01	41.7	35.65	72.13	−35.69	−0.04	96.66				4
nT275	TI275	2017-05-24T03:17:28	117 952.41	548 857 163.5	89.97	48.78	36.63	84.56	15.09	8.46	105.94	0.67	−108.8	−97.37	8

Flyby	Rev	CA UTC	CA Altitude (km)	CA Ephemeris Time	Planetocentric Longitude of the Sun (L_S)	Average Incidence (Deg)	Average Emission (Deg)	Average Phase (Deg)	Central Longitude (Deg)	Average Latitude (Deg)	Average Pixel Scale (km²)	Tilt from North Pole (Deg)	Prime Meridian Offset (Deg, E+)	Subsolar Longitude Offset (Deg, E+)	# of Longitude Bins
								Secondary 3							
T003	TI003	2005-02-15T06:57:53	1 578.974 6	161 722 737.3	301.4	10.35	20.03	13.59	−148.7	−29.78	72.81				3
T011	TI021	2006-02-27T08:25:18	1 812.311 4	194 300 783.6	315.29	15.55	32.18	18.38	7.64	−25.94	125.32				3

Table 1

(Continued)

Flyby	Rev	CA UTC	CA Altitude (km)	CA Ephemeris Time	Planetocentric Longitude of the Sun (L_S)	Average Incidence (deg)	Average Emission (deg)	Average Phase (deg)	Central Longitude (deg)	Average Latitude (deg)	Average Pixel Scale (km²)	Tilt from North Pole (deg)	Prime Meridian Offset (deg, E+)	Subsolar Longitude Offset (deg, E+)	# of Longitude Bins
T012	TI022	2006-03-19T00:05:55	1 949.351	195 998 820.6	316.02	31.28	41.31	64.45	−122.88	−26.71	48.22				3
T016	TI026	2006-07-22T00:25:26	950.385 67	206799991	320.6	45.94	28.08	59.47	4.49	−31.95	82.84				2
T017	TI028	2006-09-07T20:16:51	999.713 19	210932276	322.33	41.31	25.19	62.02	6.07	−23.94	21.08				3
T018	TI029	2006-09-23T18:58:48	960.198 92	212 309 993.5	322.92	47.84	18.47	64.22	10.72	−23.87	63.13				3
T051	TI106	2009-03-27T04:43:36	962.880 46	291 401 082.3	355.29	42.79	36.92	75.28	−107.51	−24.36	80.09				2
T057	TI113	2009-06-22T18:32:35	955.214 66	298967621	358.32	24.51	18.63	36.77	20.08	−23.85	77.08				1
T058	TI114	2009-07-08T17:04:03	966.055 3	300 344 709.3	358.86	35.98	24.14	30.34	58.67	−24.23	30.11				2
T059	TI115	2009-07-24T15:34:03	956.582 69	301 721 709.1	359.41	28.23	15.84	22.8	49.48	−23.33	22.78				1
T061	TI117	2009-08-25T12:51:37	960.837 48	304 476 763.6	0.5	30.99	28.2	12.2	45.19	−26.49	32.74				4
T063	TI122	2009-12-12T01:03:14	4 847.710 8	313 851 859.8	4.19	30.28	53.4	46.94	106.41	−27.7	87.95				2
T065	TI124	2010-01-12T23:10:36	1 074.516	316 609 901.9	5.27	29.97	62.21	45.54	90.52	−21.79	47.31				1
T066	TI125	2010-01-28T22:28:50	7 486.939 1	317 989 795.7	5.81	39.02	24.26	43.33	133.47	−23.01	74.77				2
T069	TI132	2010-06-05T02:26:27	2 042.953	328976853	10.09	34.6	25.14	30.69	139.53	−21.67	65.6				1
T077	TI149	2011-06-20T18:32:00	1 358.992 4	361 866 786.6	22.68	41.51	27.69	19.81	154.84	−24.27	40.69				2
T079	TI158	2011-12-13T20:11:23	3 583.241 3	377 079 149.2	28.41	58.13	41.55	17.39	114.06	−20.86	53.9				3
T081	TI160	2012-01-30T13:39:48	31 130.577	381 202 854.1	29.96	33.83	13.47	26.56	168.42	−19.1	71.5				2
T083	TI166	2012-05-22T01:10:11	953.990 5	390 921 076.9	33.58	42.22	24.31	21.56	128.95	−19.66	71.22				4
T084	TI167	2012-06-07T00:07:21	959.347 58	392 299 706.8	34.09	38.28	12.95	28.22	157.57	−21.09	96.53				3
T085	TI169	2012-07-24T20:03:07	1 012.449 8	396 432 253.9	35.61	36.79	10.44	32.69	158.09	−20.02	18.46				4
T087	TI174	2012-11-13T10:22:08	973.650 52	406074195	39.17	39.67	17.95	52.68	148.72	−20.43	66.26	0.01	0	−164.84	5

Secondary 4

| T009 | TI019 | 2005-12-26T18:59:26 | 10 411.572 | 188895630 | 313.01 | 38.4 | 50.36 | 27.69 | −6.32 | −47.47 | 91.9 | 1.5 | −95.39 | −50.92 | 6 |

Table 1
(Continued)

Flyby	Rev	CA UTC	CA Altitude (km)	CA Ephemeris Time	Planetocentric Longitude of the Sun (L_S)	Average Incidence (deg)	Average Emission (deg)	Average Phase (deg)	Central Longitude (deg)	Average Latitude (deg)	Average Pixel Scale (km^2)	Tilt from North Pole (deg)	Prime Meridian Offset (deg, E+)	Subsolar Longitude Offset (deg, E+)	# of Longitude Bins
T067	TI129	2010-04-05T15:50:54	7 437.318 4	323 754 719.8	8.06	53.98	50.28	15.17	18.87	−49.93	93.38	2.03	118.44	71.79	5
T119	TI235	2016-05-06T16:54:37	969.201 5	515 825 744.7	78.42	68.6	30.91	53.39	−31.99	−42.65	102.99	0.08	0.02	32.94	9
T120	TI236	2016-06-07T14:06:17	974.555 42	518 580 444.9	79.39	78.03	26.04	61.43	−30.34	−45.19	91.13	0.05	0.01	31.69	8
T121	TI238	2016-07-25T09:58:23	975.407 36	522 712 770.8	80.84	74.49	26.02	67	−55.69	−42.04	68.73	4.08	40.08	69.96	5
T123	TI243	2016-09-27T04:16:59	1 775.659 2	528221887	82.77	61.07	19.08	69.09	−41.39	−44.94	74.66	0.34	−127.27	−99.96	6
T124	TI248	2016-11-13T23:55:56	1 585.323 9	532 353 423.8	84.21	67.14	19.3	68.96	−39.1	−45.93	48.12	2.55	60.25	85.55	7

Note. A digital version of this table can be provided upon request to the first author.

Table 2
Coefficients for the Functions Displayed in Figure 9

Figure 9(A)	Coefficients								
	R^2	$\Delta I/F_0$	$P_{95\%}$	$d\Delta I/F$	$P_{95\%}$	Period (P)	$P_{95\%}$	Phase (ψ)	$P_{95\%}$
EQA Max (EQ 1)	0.567 134 084	0.001 045 799	(0.0009755, 0.001 116)	0.000 505 815	(0.0004142, 0.000 597 4)	108.714 098 7	(96.42, 121)	46.645 061 2	(34.78, 58.51)
EQA Min (EQ 1)	0.555 180 381	−0.000800664	(−0.0008791, −0.0007223)	−0.000584556	(−0.0006903, −0.0004788)	97.275 427 31	(88.58, 106)	62.814 466 72	(51.65, 73.98)
	$d(I/F)/dL_S$	$P_{95\%}$	$\Delta I/F(L_S(0))$	$P_{95\%}$					
NPA Max (EQ 2)	0.831 186 229	−2.10E-05	(−2.777e-05, −1.419e-05)	0.002 185 821	(0.001763, 0.002 608)				
NPA Min (EQ 2)	0.383 779 961	−2.79E-05	(−3.853e-05, −1.729e-05)	0.001 040 415	(0.0003801, 0.001 701)				

Figure 9(B)	Coefficients				
	R^2	$d\lambda/dL_S$	$P_{95\%}$	$\lambda(L_S(0))$	$P_{95\%}$
EQA Max (EQ 3)	0.534 429 624	9.02E-05	(−0.0002733, 0.000 453 8)	0.880 850 658	(0.8689, 0.892 8)
EQA Min (EQ 3)	0.952 738 203	−2.19E-05	(−0.000729, 0.000 685 3)	0.519 985 156	(0.4967, 0.543 3)
NPA Max (EQ 3)	0.618 118 166	0.004 308 898	(0.000602, 0.008 016)	0.625 063 359	(0.3945, 0.855 6)
NPA Min (EQ 3)	0.898 577 491	5.36E-06	(−0.005123, 0.005 134)	0.497 419 496	(0.1785, 0.816 4)

Note. The columns labeled $P_{95\%}$ are the 95th percentile confidence bounds of the coefficients in the respective columns to the left.
EQ1) $\Delta I/F = \Delta I/F_0 + d\Delta I/F \sin(L_S/P + \psi)$
EQ2) $\Delta I/F = \Delta I/F(L_S(0)) + d(I/F)/dL_S \times L_S$
EQ3) $\lambda = \lambda(L_S(0)) + d\lambda/(dL_S) \times L_S$

ORCID iDs

N. W. Kutsop ⓘ https://orcid.org/0000-0001-7188-9044
A. G. Hayes ⓘ https://orcid.org/0000-0001-6397-2630
P. M. Corlies ⓘ https://orcid.org/0000-0002-6417-9316
S. Le Mouélic ⓘ https://orcid.org/0000-0001-5260-1367
J. I. Lunine ⓘ https://orcid.org/0000-0003-2279-4131
C. A. Nixon ⓘ https://orcid.org/0000-0001-9540-9121
P. Rannou ⓘ https://orcid.org/0000-0003-0836-723X
S. Rodriguez ⓘ https://orcid.org/0000-0003-1219-0641
M. T. Roman ⓘ https://orcid.org/0000-0001-8206-2165
C. Sotin ⓘ https://orcid.org/0000-0003-3947-1072
T. Tokano ⓘ https://orcid.org/0000-0002-7518-9245

References

Achterberg, R. K., Conrath, B. J., Gierasch, P. J., Flasar, F. M., & Nixon, C. A. 2008, Icar, 197, 549
Achterberg, R. K., Gierasch, P. J., Conrath, B. J., Michael Flasar, F., & Nixon, C. A. 2011, Icar, 211, 686
Acton, C., Bachman, N., Semenov, B., & Wright, E. 2018, P&SS, 150, 9
Ádámkovics, M., Mitchell, J. L., Hayes, A. G., et al. 2016, Icar, 270, 376
Battalio, J. M., & Lora, J. M. 2021a, NatAs, 5, 1139
Battalio, J. M., & Lora, J. M. 2021b, GeoRL, 48, e94244
Battalio, J. M., Lora, J. M., Rafkin, S., & Soto, A. 2022, Icar, 373, 114623
Brown, M. E., Bouchez, A. H., & Griffith, C. A. 2002, Natur, 420, 795
Brown, R. H., Baines, K. H., Bellucci, G., et al. 2004, SSRv, 115, 111
Caldwell, J., Cunningham, C. C., Anthony, D., et al. 1992, Icar, 97, 1
Charlot, P., Jacobs, C. S., Gordon, D., et al. 2020, A&A, 644, A159
Clark, R. N. B., Robert, H., Lytle, D. M., & Hedman, M. 2018, PDSS, http://atmos.nmsu.edu/data_and_services/atmospheres_data/Cassini/vims.html
Cleveland, W. S. 1979, Journal of American Statistical Association, 74, 829
Corlies, P., McDonald, G. D., Hayes, A. G., et al. 2021, Icar, 357, 114228
de Kok, R., Irwin, P. G. J., Teanby, N. A., et al. 2010, Icar, 207, 485
Filacchione, G., Capaccioni, F., McCord, T. B., et al. 2007, Icar, 186, 259
Flasar, F. M., & Achterberg, R. K. 2009, RSPTA, 367, 649
Fletcher, L. N., Kaspi, Y., Guillot, T., & Showman, A. P. 2020, SSRv, 216, 30
Gierasch, P. J. 1975, JAtS, 32, 1038
Goody, R., West, R., Chen, L., & Crisp, D. 1989, JQSRT, 42, 539
Griffith, C. A., McKay, C. P., & Ferri, F. 2008, ApJ, 687, L41
Horinouchi, T., Murakami, S. Y., Satoh, T., et al. 2017, NatGe, 10, 646
Hörst, S. M. 2017, JGRE, 122, 432
Hourdin, F., Talagrand, O., Sadourny, R., et al. 1995, Icar, 117, 358
Jennings, D. E., Achterberg, R. K., Cottini, V., et al. 2015, ApJ, 804, L34
Kelland, J., Turtle, E., Rodriguez, S., Hayes, A., & Corlies, P. 2018, in 42nd COSPAR Scientific Assembly (Pasadena, CA), B5.2-43-18
Knowles, B. 2016, Planetary Data System, Ring-Moon Systems Node, https://pds-rings.seti.org/cassini/iss/
Larson, E. J. L., Toon, O. B., West, R. A., & Friedson, A. J. 2015, Icar, 254, 122
Lavvas, P., Yelle, R. V., & Griffith, C. A. 2010, Icar, 210, 832
Lavvas, P. P., Coustenis, A., & Vardavas, I. M. 2008a, P&SS, 56, 27
Lavvas, P. P., Coustenis, A., & Vardavas, I. M. 2008b, P&SS, 56, 67
Le Mouélic, S., Cornet, T., Rodriguez, S., et al. 2019, Icar, 319, 121
Le Mouélic, S., Rannou, P., Rodriguez, S., et al. 2012, P&SS, 60, 86
Le Mouélic, S., Rodriguez, S., Robidel, R., et al. 2018, Icar, 311, 371
Lebonnois, S., Burgalat, J., Rannou, P., & Charnay, B. 2012, Icar, 218, 707
Lebonnois, S., Flasar, F. M., Tokano, T., & Newman, C. E. 2014, in Titan, ed. I Müller-Wodarg et al. (Cambridge: Cambridge Univ. Press), 122
Lora, J. M., Lunine, J. I., & Russell, J. L. 2015, Icar, 250, 516
Lora, J. M., Tokano, T., Vatant d'Ollone, J., Lebonnois, S., & Lorenz, R. D. 2019, Icar, 333, 113
Lorenz, R. D., Smith, P. H., Lemmon, M. T., et al. 1997, Icar, 127, 173
Lorenz, R. D., Young, E. F., & Lemmon, M. T. 2001, GeoRL, 28, 4453
Luz, D., & Hourdin, F. 2003, Icar, 166, 328
Mayo, L. A., & Samuelson, R. E. 2005, Icar, 176, 316
McCord, T. B., Hayne, P., Combe, J.-P., et al. 2008, Icar, 194, 212
Mitchell, J. L., Pierrehumbert, R. T., Frierson, D. M. W., & Caballero, R. 2006, PNAS, 103, 18421
Newman, C. E., Lee, C., Lian, Y., Richardson, M. I., & Toigo, A. D. 2011, Icar, 213, 636
Newman, C. E., Richardson, M. I., Lian, Y., & Lee, C. 2016, Icar, 267, 106
Nixon, C. A., Achterberg, R. K., Ádámkovics, M., et al. 2016, PASP, 959, 018007
Nixon, C. A., Lorenz, R. D., Achterberg, R. K., et al. 2018, P&SS, 155, 50
O'Donoghue, J., Moore, L., Bhakyapaibul, T., et al. 2021, Natur, 596, 54
Penteado, P. F., Griffith, C. A., Tomasko, M. G., et al. 2010, Icar, 206, 352
Pollack, J. B., & McKay, C. P. 1985, JAtS, 42, 245
Rages, K., & Pollack, J. B. 1983, Icarus, 55, 50
Rannou, P. 2000, Icar, 147, 267
Rannou, P., Hourdin, F., McKay, C. P., & Luz, D. 2004, Icar, 170, 443
Rannou, P., Le Mouélic, S., Sotin, C., & Brown, R. H. 2012, ApJ, 748, 4
Rannou, P., Toledo, D., Lavvas, P., et al. 2016, Icar, 270, 291
Rodriguez, S., Le Mouelic, S., Rannou, P., et al. 2009, Natur, 459, 678
Rodriguez, S., Le Mouélic, S., Rannou, P., et al. 2011, Icar, 216, 89
Roe, H. G. 2012, AREPS, 40, 355
Roe, H. G., de Pater, I., Macintosh, B. A., et al. 2002, Icar, 157, 254
Roman, M. T., West, R. A., Banfield, D. J., et al. 2009, Icar, 203, 242
Rossow, W. B., & Williams, G. P. 1979, JAtS, 36, 377
Saur, J., Duling, S., Roth, L., et al. 2015, JGRA, 120, 1715
Savitzky, A., & Golay, M. J. E. 1964, AnaCh, 36, 1627
Seignovert, B., Le Mouélic, S., Brown, R. H., et al. 2019, CaltechDATA, Titan's Global Map Combining VIMS and ISS Mosaics, https://data.caltech.edu/records/1173
Seignovert, B. t., Rannou, P., West, R. A., & Vinatier, S. 2021, ApJ, 907, 36
Smith, B. A., Soderblom, L., Batson, R. M., et al. 1982, Sci, 215, 504
Smith, B. A., Soderblom, L., Beebe, R. F., et al. 1981, Sci, 212, 163
Sromovsky, L. A., Suomi, V. E., Pollack, J. B., et al. 1981, Natur, 292, 698
Stiles, B. W., Kirk, R. L., Lorenz, R. D., et al. 2008, AJ, 135, 1669
Teanby, N. A., de Kok, R., & Irwin, P. G. J. 2009, Icar, 204, 645
Teanby, N. A., Irwin, P. G., Nixon, C. A., et al. 2012, Natur, 491, 732
Teanby, N. A., Irwin, P. G. J., & de Kok, R. 2010, P&SS, 58, 792
Tokano, T. 2010, P&SS, 58, 814
Tokano, T. 2011, Sci, 331, 1393
Tokano, T., & Neubauer, F. M. 2005, GeoRL, 32, L24203
Tomasko, M. G., & Smith, P. H. 1982, Icar, 51, 65
Turtle, E. P., Perry, J. E., Barbara, J. M., et al. 2018, GeoRL, 45, 5320
West, R. A., Del Genio, A. D., Barbara, J. M., et al. 2016, Icar, 270, 399
West, R. A., Seignovert, B., Rannou, P., et al. 2018, NatAs, 2, 495
Yung, Y. L., Allen, M., & Pinto, J. P. 1984, ApJS, 55, 465